Journal of The
Electrochemical Society

Advanced Balancing of High-Energy Lithium Ion Cells Comprising Lithium-Rich Layered Oxide and a-Si/CuSi Nanowire Using a Cathode Pre-Lithiation Additive

To cite this article: William W. Chesson *et al* 2024 *J. Electrochem. Soc.* **171** 120525

Journal of The Electrochemical Society, 2024 **171** 120525

Advanced Balancing of High-Energy Lithium Ion Cells Comprising Lithium-Rich Layered Oxide and a-Si/CuSi Nanowire Using a Cathode Pre-Lithiation Additive

William W. Chesson,[1] Florian Klein,[2] Thomas Diemant,[1,3] Annika Regitta Schür,[1,3] Claudia Pfeifer,[2] Paul Drews,[2] Zenonas Jusys,[1,3,4] R. Jürgen Behm,[4] Mika Lindén,[5] Hugh Geaney,[6] Kevin Ryan,[6] Matthias Kuenzel,[1,3] Dominic Bresser,[1,3] Peter Axmann,[2] and Stefano Passerini[1,3,*,z]

[1]*Helmholtz Institute Ulm (HIU), D-89081 Ulm, Germany*
[2]*Center for Solar Energy and Hydrogen Research Baden-Württemberg (ZSW), D-89081 Ulm, Germany*
[3]*Karlsruhe Institute of Technology (KIT), D-76021 Karlsruhe, Germany*
[4]*Institute of Theoretical Chemistry, Ulm University, D-89081 Ulm, Germany*
[5]*Institute for Inorganic Chemistry II, Ulm University, D-89081 Ulm, Germany*
[6]*Bernal Institute and Department of Chemical Sciences, University of Limerick, Limerick V94 T9PX, Ireland*

Advances in lithium-ion battery (LIB) research have strived for high-energy, safe, and sustainable materials. Li-rich $Li_{1.2}Ni_{0.2}Mn_{0.6}O_2$ (LRNM) cathodes have shown great promise with high voltages and excellent specific capacities. Obstacles preventing the viability and commercialization of LRNM are the initial capacity loss of roughly 30% and rapid voltage decay upon cycling. Herein, lithium oxalate ($Li_2C_2O_4$) is investigated as a pre-lithiation additive to utilize the first-cycle lithium re-intercalation losses of LRNM to compensate the irreversible lithium consumption in graphite and high-capacity a-Si on copper silicide nanowire (a-Si/CuSi NW) anodes. Specifically, the decomposition process of $Li_2C_2O_4$ as well as the interaction between the electrode components inside the cell are comprehensively examined. This concept allows us to extend the cycle life of graphite||LRNM cells at 1 C from less than 500 cycles (142 mAh g^{-1}, 78%) to more than 900 cycles (143 mAh g^{-1}, 82%) before reaching the 80% capacity retention threshold. Finally, LRNM electrodes with a precisely balanced concentration of $Li_2C_2O_4$ are prepared in order to compensate the high irreversible losses of a-Si/CuSi NW anodes, achieving a capacity retention of almost 50% with a remaining specific capacity of 82 mAh g^{-1} after 400 cycles in high-energy a-Si/CuSi NW||LRNM lithium-ion cells.
 [DOI: 10.1149/1945-7111/ad9bf2]

Manuscript submitted September 26, 2024; revised manuscript received December 4, 2024. Published December 19, 2024.

Supplementary material for this article is available online

The transition of the global energy economy is well underway. Countries are eager to shift their energy reliance away from the traditional, non-renewable sources that the world has come to depend on such as coal, oil, and gas to cleaner, renewable energy sources, mainly wind, solar, hydro power, and biomass.[1] In addition to the shift in global energy production, the transportation industry has indeed begun its own transition to new-energy vehicles (NEVs) with almost every major auto manufacturer announcing plans for battery electric vehicle (BEV) production.[2,3] Taken together, this has driven the need for efficient energy storage solutions that are practical in terms of their gravimetric and volumetric energy and power densities. The most promising technology to solve this problem is the lithium-ion battery (LIB). Although graphite is the current state-of-the-art anode active material in LIBs, silicon (Si) based anode active materials are of great interest in academia and industry due to the exceptional theoretical capacity that Si offers when it is alloying with lithium (372 mAh g^{-1} for graphite vs 3,579 mAh g^{-1} for Si). However, pure Si suffers from volume expansion of almost 300% when alloying with lithium, causing severe challenges with respect to cycle life.[4,5]

Among various micro structuring approaches for Si-based anode materials, Si nanowires (NWs) have attracted much attention.[6,7] The NW structure allows for the expansion of the Si active material upon lithiation without cracking or losing connection to the current collector. NW structures overcome the inherently slow Li^+ diffusion by shortening the diffusion path to the electrolyte and additionally enable better electron transport given their 1D structure.[6–8] Together with the provided mobility and flexibility of the structure, these attributes allow to overcome the obstacles of planar Si electrodes such as pulverization and active material loss that ultimately lead to capacity failure.[9] An emerging and attractive NW based architecture consists of electrochemically inactive metal or silicide NWs coated with active Si. This allows the impact of volume expansion associated with lithiation/delithiation of Si to be mitigated, while ensuring good electronic conductivity within the anode. An example of this arrangement is a copper silicide ($Cu_{15}Si_4$) NW substrate, which is coated with an amorphous Si (a-Si) layer via chemical vapor deposition. This material has been reported in the work of Stokes et al.[10] and shows promising performance with regard to its very high discharge capacity and cycle life.

Layered-oxides like lithium cobalt oxide (LCO), lithium nickel manganese cobalt oxide (NMC), and lithium nickel cobalt aluminium oxide (NCA) are among the dominant cathode active materials due to their high specific capacities, but are expensive. Furthermore, they contain a significant share of Co as critical raw material and can suffer from thermal runaway issues, especially when the nickel content is increased to gain higher capacity.[11] In this regard, Li-rich layered oxides (LRLOs) are a better option than Ni-rich NMC chemistries, as they contain more than one Li atom per unit cell and thus offer additional capacity. Their structure can best be described as a coexistence of two phases, Li_2MnO_3 and $LiMO_2$ (M = Ni, Co, Mn).[12] Furthermore, the much higher relative fraction of environmentally friendly and abundant manganese, e.g., in $Li_{1.2}Ni_{0.2}Mn_{0.6}O_2$ (LRNM), makes them an attractive alternative to Ni-rich materials.[13]

In addition, LRNM is a promising material because of its relatively high voltage and specific capacity, leading to excellent energy density. The potentially very high reversible capacity of 250 mAh g^{-1} or more originates from the activation of the Li_2MnO_3 component that follows the Ni^{2+}/Ni^{4+} oxidation.[14] During the initial

*Electrochemical Society Fellow.
[z]E-mail: stefano.passerini@kit.edu

high-voltage charge of LRNM, additional capacity is accessed via an oxygen anion redox reaction which is partially irreversible, resulting in the loss of lattice oxygen from the structure and even O_2 evolution.[15] The activation of this oxygen anion redox process contributes substantially to the irreversible loss of lithium observed for LRLOs in the first cycle, however, it is also the main driver for the exceptionally high capacity.[16] Furthermore, the loss of oxygen triggers cation mixing especially in the surface region of the cathode active material, where nickel atoms occupy the 3a lithium sites. Over the course of several cycles, the layered structure transforms into a spinel phase, and then eventually an electrochemically inactive rock-salt structure is formed.[17,18] This structural transformation is irreversible and one of the main causes for voltage fading and capacity loss observed during extended cycling.[19,20]

Strategies to avoid or at least slow down the voltage decay of LRMOs have been numerous. Changes to material composition have been successful in reducing voltage decay such as removing cobalt, as also adopted herein with LRNM, and increasing the ratio of Ni to Mn.[13,21] Limiting the voltage range after initial Li_2MnO_3 activation to below 4.5 V vs Li^+/Li has also been successful, however, with the drawback of decreased reversible capacity from the beginning.[22] Cation substitution with elements like Al^{3+} and Mg^{2+}, having higher bonding energies with lattice oxygen, are proposed to have a positive effect on voltage decay.[23] Lastly, surface modification of particles can show benefits like decreasing cationic disorder in the lattice, phase-transition suppression, and electrode-electrolyte interface stabilization.[24,25]

To mitigate the irreversible first cycle capacity loss on anode side, pre-lithiation has been a successful strategy.[26,27] One of the most promising pre-lithiation methods is the introduction of sacrificial lithium salts at the positive electrode.[28] Specifically, lithium oxalate ($Li_2C_2O_4$) is a prime candidate for high-voltage systems like LRNM because of its high decomposition potential at around 4.4 to 4.7 V vs Li^+/Li, its specific capacity and especially the volatile decomposition products. Theoretically, $Li_2C_2O_4$ will be oxidized by the following reaction:

$$Li_2C_2O_4 \rightarrow 2\,Li^+ + 2\,e^- + 2\,CO_2$$

Solchenbach et al.[29] have reported the use of up to 5 wt% $Li_2C_2O_4$ with LNMO spinel cathode material in combination with graphite and Si-C anodes and a 1 M $LiPF_6$ in EC:EMC (3:7 wt/wt) electrolyte with very promising results. The LNMO spinel has a voltage plateau at about 4.7 V vs Li^+/Li which was successfully extended via the addition of the oxalate to the cathode slurry mixture during electrode manufacturing process. Compared to LNMO spinel materials, which have a very small irreversible first cycle capacity loss, LRLOs suffer from losses up to 40%.[30] To the best of our knowledge, $Li_2C_2O_4$ has not been examined as agent for compensating Li loss in full cells with LRLO cathode materials in combination with high Si content anodes.

Herein, we address one of the biggest challenges of Si || LRLO full-cells by adding additional Li as sacrificial Li salt in the form of $Li_2C_2O_4$ to the electrode. The additional Li is released during the decomposition of $Li_2C_2O_4$ in the first charge. A comprehensive combination of microscopic and spectroscopic techniques was employed to develop a more complete understanding of the electrode materials, the decomposition of the pre-lithiation additive and specifically the interaction between the electrode components inside the cell. We prove that pre-lithiation with $Li_2C_2O_4$ can mitigate not only the high irreversible first cycle capacity, but also double the lifetime of graphite||LRNM full-cells. The amount of additional Li has to be adjusted carefully to fully compensate the irreversible capacity loss of the anode, which is strongly depending on the active material (graphite < Si), but simultaneously avoid plating of Li metal on the anode in the fully charged state. By carefully balancing the concentration of $Li_2C_2O_4$, we demonstrate that LRNM full-cells with a-Si/CuSi NW anodes can compensate the high irreversible capacity losses of a-Si and enable high energy LIBs.

Experimental

Material preparation.—Different synthesis routes were followed to prepare two types of LRNM materials. In the first route, LRNM was obtained from a mixed nickel-manganese hydroxide precursor ($Ni_{0.2}Mn_{0.6}(OH)_{1.6}$) which was synthesized by co-precipitation of nickel sulfate (nickel(II) sulfate hexahydrate, >99%, Sigma-Aldrich) and manganese sulfate (manganese(II) sulfate monohydrate, >98%, Sigma-Aldrich). An aqueous solution of mixed 1 M $NiSO_4$ and $MnSO_4$ (molar ratio Ni:Mn = 1:3) was added to a 1 M aqueous LiOH solution (lithium hydroxide monohydrate, battery grade, AlfaAesar) under constant stirring (400 rpm) at room temperature and under inert-gas (Ar) atmosphere. Milky, green precipitates formed immediately and throughout the mixing phase while being stirred overnight at 400 rpm. The $Ni_{0.2}Mn_{0.6}(OH)_{1.6}$ precipitate was then washed with deionized water until neutralization and finally filtered. The solids were dried overnight at 80 °C, ground in a mortar, and then mixed with +8% excess LiOH dispersed in acetone in a 1 mL:1 g precursor ratio to compensate any potential lithium loss during calcination. Mixing was carried out in a ball mill for 4 h. The precursor was dried, ground briefly, and then calcined at 480 °C for 5 h. After cooling down overnight, the powder was pressed into 1 gram pellets which were calcined again at 950 °C for 24 h, then immediately quenched in water and rinsed dry with acetone. Finally, the pellets were ground in a mortar and sieved to particles smaller than 40 μm.

The second type of LRNM with spherical particle architecture was synthesized via lithiation and calcination of a coprecipitated Mn-Ni-carbonate precursor with a Mn:Ni ratio of 3:1 in kg-scale. The precursor was mixed with 2% excess of $LiOH{\cdot}xH_2O$ (Roth) and an adequate amount of Millipore water to obtain a highly viscous slurry. The mixture was dried overnight at 120 °C and then calcined with a final calcination temperature of 900 °C under air. Subsequently, the material was post-treated with water as reported in a previous publication. LRNM (0.80 kg) was added under vigorous stirring into hot Millipore water (2 L), stirred for 20 min and then separated. The procedure was repeated two times before the material was dried at 120 °C and calcined at 300 °C under air. The final product was sieved (mesh size: 32 μm) to remove possible agglomerates.

Electrode preparation.—LRNM electrodes without $Li_2C_2O_4$ additive were prepared by first mixing the active material (LRNM), the binder (polyvinylidene difluoride, PVdF, Solef 6020, SOLVAY), and conductive carbon (Super-C 65, SPC-65, IMERYS) at a ratio of 85:5:10 for the solids, before dispersing/dissolving the mixture in N-methyl-2-pyrrolidone (NMP, >99.5%, Alfa-Aesar, solid content 33 wt%). All components were added into a ball mill jar and mixed by ball milling three times for a total of 75 min. The slurry was then cast on aluminium foil using a doctor blade with a fixed gap size of 60 μm on a table-top coating machine. The coated electrode was dried in an oven at 60 °C overnight to evaporate the NMP and transferred to the dry-room for cutting and pressing.

Circular electrodes were cut out using a puncher (Hohsen) with 12 mm diameter. Subsequently, electrodes were pressed using a hydraulic cylinder with a force of 100 kN and then dried under vacuum (about 10^{-3} mbar) at 120 °C for 12 h. The process was the same for LRNM with the oxalate additive (Alfa-Aesar) except that the active material, binder, and SPC-65 weight fractions were reduced to accommodate the total weight fraction of oxalate. The mass ratio of the active material to carbon to binder was kept uniform throughout. Electrodes were prepared with 10 wt% $Li_2C_2O_4$ for half-cell tests and full-cell tests with graphite anodes, and with 3 wt% $Li_2C_2O_4$ for full-cell tests with a-Si/CuSi NW anodes. A calculation was carried out to determine the optimal weight percent of additive in the cathode to be in coordination with the silicon loading of 0.15 mg cm^{-2} of the anode. In order for the LRNM cathode to be appropriately balanced with the supplied SiNW anode,

then the cathode active material loading was determined to be from 1.75 to 1.81 mg cm^{-2} with 3 wt% $Li_2C_2O_4$ additive.

Graphite anodes were prepared using spheroidized natural graphite (WELLCOS) in a mass ratio of 95:1:1:3 with conductive carbon (Super-C 45, IMERYS), sodium carboxyethyl cellulose (CMC, WALOCEL) and styrene-butadiene rubber (SBR, Dow Chemical). The slurry (55 wt% solid content) was made using water as solvent and dispersant in a planetary shear mixer (KK-400WE, KURABO Mazerustar). The electrodes were punched into 12 mm disks and after that pressed using a hydraulic press with a force of 500 N for 10 s. The pressed electrodes were dried under vacuum ($<10^{-3}$ mbar) in a Büchi oven at 110 °C. The graphite electrodes were stored in a glovebox.

The Si-composite nanowire anodes (a-Si/CuSi NW) consist of an amorphous coating of Si (a-Si) that was formed by a plasma-enhanced chemical vapour deposition (PECVD) process carried out by Smit Thermal Solutions at the surface of solvent-vapour grown copper silicide ($Cu_{15}Si_4$) NWs on a dendritic copper foil substrate serving as the current collector.[10] The circular a-Si/CuSi NW anodes were punched into 12 mm disks with a hand-punch. These anodes did not undergo a pressing process to avoid damaging the NWs. The a-Si/CuSi NW anodes were dried, weighed, and stored using the same procedure as for the graphite anodes. A specific charge capacity of 3,579 mAh g^{-1} was assumed for the a-Si/CuSi NW anodes. The mass loading of the Si active material ranged from 0.137 to 0.158 mg cm^{-2}.

Three-electrode cells (T-cells) were used for all electrochemical tests. Cells were assembled in an Ar-filled glove box (H_2O and O_2 content <0.1 ppm). In the case of cells with Li-metal counter electrodes, a 12 mm diameter, 500 μm thick Li-metal disk was inserted on the negative side. A 13 mm diameter porous glass fiber separator (GF/D, WHATMAN) was used and soaked either with 130 μL of electrolyte LP30 (1 M $LiPF_6$ in EC:DMC, 1:1, w:w, SOLVIONIC) for half-cells and full-cells with graphite anodes or with the same volume of a mixture of LP30 with fluoroethylene carbonate (FEC) or vinylene carbonate VC (1 M $LiPF_6$ + 3 wt% FEC/VC in EC:DMC, 1:1, w:w, SOLVIONIC) for full-cells with a-Si/CuSi NW anodes.

For the pouch cell assembly, graphite anodes from the HIU pre-pilot scale coating line with an areal capacity of 1.62 mAh cm^{-2} were used. The cathode electrodes were made in a similar manner, as already described, but without using a ball-mill to preserve the spherical particle morphology of the kg-scale LRNM material. A homogeneous slurry of the spherical LRNM material, PVdF (Solef 5130, SOLVAY), and SPC-65 (IMERYS) (dry ratio of 85:5:10) dispersed in an adequate amount of NMP (Sigma Aldrich, solid content 32 wt%) was coated on an aluminium foil using a doctor blade. The oxalate containing electrodes were similarly prepared with 5 wt% and 10 wt% $Li_2C_2O_4$ (Alfa-Aesar), keeping the solid content and the dry ratio of the LRNM, binder and conductive carbon constant. To avoid large agglomerates, $Li_2C_2O_4$ was ground and sieved in advance (mesh size of 45 μm), but not ball milled together with the active material to keep the spherical shape of the LRNM particles. The electrodes were calendared after drying to a thickness of 50 μm (100 °C) and transferred into the dry room (dew point <−60 °C) together with the anodes. Electrodes were punched from the electrode sheets (anode: 65×40 mm^2, cathode: 63×38 mm^2) and the tabs were cleaned with laser ablation. The prepared electrodes were dried under vacuum at 130 °C, subsequently wrapped with separator foil (Celgard 2325) and packed into pouch bags. Before the cells were filled with the electrolyte (1 M $LiPF_6$ in EC:DMC, 1:1, w:w, SOLVIONIC, 1.2 mL) and sealed in an Ar-filled glovebox (MBraun, H_2O and O_2 <0.1 ppm), they were dried again for 16 h under vacuum at 80 °C.

Physicochemical characterization.—FIB-SEM & EDX measurements on pristine and cycled electrodes were carried out on a Crossbeam XB340 (ZEISS) field-emission scanning electron microscope equipped with an integrated energy-dispersive X-ray spectrometer (XmaxXtreme, Oxford Instruments) and a focused-ion beam (FIB) system with a Ga-source (Capella, ZEISS) system. Imaging was performed at a working distance of approximately 5 mm, using a secondary electron (SE2) detector and an accelerating voltage of 5 kV. FIB milling and polishing of electrode cross-sections were performed using ion currents of 30 nA and 3 nA, respectively. All samples were introduced into the vacuum (10^{-7} mbar) of the microscope using an air-tight sample transfer shuttle (SEMILAB) which was loaded inside the glove box. Cycled electrodes were rinsed with DMC to remove remains of the electrolyte and dried overnight inside a glove box.

X-ray photoelectron spectroscopy (XPS) was performed on LRNM electrodes and LRNM electrodes with 10 wt% $Li_2C_2O_4$ in the pristine state and after one charge/discharge cycle at C/20. The pristine and recovered electrodes were mounted on the sample plate with sticky carbon tape inside a glove box and then transferred to the load lock of the XPS machine in an air-tight container. The measurements were performed at a Phoibos 150 XPS spectrometer (Specs) equipped with a delay line detector and using monochromatized Al K_α radiation (400 W, 15 kV) as well as pass energies of 90 and 30 eV at the analyser for the survey and detail scans, respectively. In addition to the detail measurements in the C1s, O1s, F1s and P2p regions, detail spectra were also recorded in the Mn3s region (pass energy 60 eV). Peak fitting was carried out using the CasaXPS software with Shirley-type backgrounds and 70% Gaussian–30% Lorentzian peak profile functions. The binding energy was calibrated at the main C1s peak (C-C/C-H at 284.8 eV) as reference.

Special electrodes were prepared to perform differential electrochemical mass-spectrometry (DEMS) analysis of the LRNM electrodes without and with 10 wt% $Li_2C_2O_4$. The slurries prepared as above were coated onto a substrate made of a fluorinated ethylene propylene (FEP) membrane with a sputtered aluminium coating. The coated slurry was dried in the same manner as before and 12 mm diameter electrodes were punched out manually. The cell assembly (modified Swagelok-type T-cell with a PEEK cylinder and a PEEK cup sealed with Teflon and Parafilm gaskets) was described previously in detail.[31] The analysis was performed under galvanostatic conditions at an approximated C rate of C/10 from 2.5–4.95 V vs Li^+/Li in an Ar-filled glovebox at about 20 °C.

The gas formation was quantified by analysing the change in the cell volume using the Archimedes' principle. Since the cell mass remained constant during cycling due to mass conservation, the gas volume is proportional to the changes in the buoyant force of the cells in a liquid. Detailed theoretical background is reported in literature.[32] In a first step, the cells were weighted precisely. Subsequently, they were submerged before and after cycling into Millipore water (20 °C, 0.055 μS cm^{-2} @ 25 °C) with the help of small wires, which are connected to a balance (Mettler-Toledo,[33] XP205 and density kit). The experimental values of the cell volume are mean values of at least six cells.

For the Raman and SEM studies of the pouch cell electrodes, a small piece of the latter was polished with an Ar^+ ion beam milling system (IM4000Plus, Hitachi) to prepare the cross-section. SEM characterization was conducted using a Leo 1530VP (Zeiss) equipped with a Schottky thermal field emitter source. Imaging was performed at 5 kV accelerating voltage with an Everhardt-Thornley detector. Raman spectroscopy was carried out with an alpha300 R confocal Raman microscope (WITec) equipped with an 100x objective (Zeiss) and a Nd:YAG laser (532 nm). The laser power was adjusted to 1.5 mW after microscope transit. The spectrometer was equipped with a grating (600 lines mm^{-1}) and a CCD camera. The spectra of the electrode mappings were analyzed and evaluated with the software Project FIVE (WITec).

Mercury intrusion porosity experiments were conducted with a PASCAL 140–40 Series (Porotec) porosimeter. The cells were disassembled in an argon-filled glovebox (MBraun, H_2O and O_2 < 0.1 ppm) and washed with DMC to remove any electrolyte residues. Subsequently, the electrodes were cut into small pieces

and filled into the sample holder. The porosity measurements were conducted in the pressure region between 0.01 MPa and 375 MPa. For the evaluation of the data, a contact angle of 140° following DIN ISO Norm 15901:2016 was used. More details are reported in literature.[34]

Electrochemical characterization.—Galvanostatic cycling was performed on a battery cycler (Maccor 4300) in a climatic chamber (Binder) kept at a constant temperature of 20 °C. All cells underwent a 12 h rest step before a constant current was applied for cycling. The potential windows were 2.5–4.9 V for the first cycle and 2.5–4.8 V for the following cycles in half-cells, and 2.0–4.9 V for the first cycle and 2.0–4.8 V for the following cycles and C rates up to C/2, and 1.8–4.8 V for higher C rates (1 C, 2 C, and 5 C) in full-cells (1 C = 250 mA g^{-1}).

Galvanostatic cycling of the pouch cells was performed on a battery cycler (BaSyTec) at a constant temperature of 40 °C (climate chamber, Binder) between 2.0 and 4.9 V at dis-/charge rates of C/20 (1st cycle) and C/10 (2nd & 3rd cycle), hereinafter referred to as formation. The presented capacities are mean values of at least six cells.

Results and Discussion

Herein, $Li_2C_2O_4$ was used as a pre-lithiation additive in LRNM cathodes in order to create an additional Li reservoir and balance the irreversible first cycle capacity loss. To investigate the influence of the pre-lithiation additive, it is relevant to discuss first the shape of the potential profile of LRNM in general (Fig. 1). Upon initial charging up to about 4.45 V vs Li^+/Li, the potential shows a sloped profile with a charge capacity of around 105 mAh g^{-1} (Fig. 1a), where lithium is removed from the transition metal layers in the $LiMO_2$ regions, during which the $Ni^{2+/4+}$ oxidation occurs. In Fig. 1b, the potential profile of the first cycle is compared to the differential capacity with respect to voltage. For LRNM, there are three oxidation peaks O1–O3, where O1 and O2 are lying in this sloped potential region and most likely correspond to the oxidation of $Ni^{2+/3+}$ and $Ni^{3+/4+}$, respectively.[35] The subsequent process O3 is characterized by the potential plateau in the range of 4.45–4.6 V vs Li^+/Li, in which another 195 mAh g^{-1} of capacity is provided. The reaction mechanism leading to this plateau is subject of ongoing research, due to its higher than theoretical contribution, and it has been proposed to be attributable to the oxidation of lattice oxygen in the Li_2MnO_3 domains during de-lithiation to $\alpha MnO_2 \cdot (1-\alpha)Mn[O^{4/3-}]_3$, resulting in the partial release of oxygen species from the crystal lattice.[36] However, it has also been proposed that there is concomitant $Mn^{4+/3+}$ reduction, allowing for more oxygen removal from the lattice.[35] The scientific consensus is that oxygen lattice vacancy formation is the main contribution to this potential plateau.[35,37] In Figs. 1b, 1d, this is represented by the oxidation peak O3, possibly overlapping with a small contribution from electrolyte oxidation, i.e., the decomposition of the organic solvents in LP30 at high potentials.[38] The individual reduction features of the discharge processes, in which re-lithiation of the cathode active material is taking place, are visible in the differential capacity plot (Fig. 1b), which gives more insights than only the continuously sloping potential profile in Fig. 1a. When looking at the differential capacity plot, the reduction peak R1 is the reversible $O^{2-}/O^{(2-x)-}$ reduction from the oxygen that remained trapped in the lattice structure. The R2 and R3 peaks can be attributed to the reversible reduction of $Ni^{4+}/Ni^{3+}/Ni^{2+}$ and the re-lithiation of the newly formed $LiMnO_2$ phase.[36,37] Comparing this with an LRNM electrode containing 10 wt% $Li_2C_2O_4$, the appearance of a second voltage plateau at about 4.7–4.8 V vs Li^+/Li indicates that $Li_2C_2O_4$ decomposition does not occur prior to the activation process of Li_2MnO_3 domains of LRNM at 4.5 V vs Li^+/Li. This is confirmed by the dQ/dV plot in Fig. 1b, in which the decomposition of the $Li_2C_2O_4$ is clearly seen as peak O4 for the pre-lithiated cathode, but is missing in the curve of the uncoated cathode. The reduction portions of the dQ/dV plots for both the pre-lithiated and non-pre-lithiated LRNM cathodes are quite similar with a small notable exception. For the pre-lithiated cathode, the R1 peak shifts to slightly lower potentials and merges with the R2 peak. This slight shift of the R1 peak to the left possibly indicates hindrance of oxygen reduction possibly due to a surface film of side reaction products based on the CO_2 gas evolved upon decomposition of $Li_2C_2O_4$, as will be discussed in more detail later on.

Although the decomposition of $Li_2C_2O_4$ seemingly does not have an immediate impact on the electrochemical profiles from the second cycle onwards (Fig. 1c), it should theoretically affect the electrode structure. Therefore, SEM analysis was carried out on pristine electrodes of LRNM with 0 wt% and 10 wt% $Li_2C_2O_4$ as well as on electrodes of the same composition after one full galvanostatic cycle at C/20. The LRNM electrodes with 0 wt% $Li_2C_2O_4$ (Figs. 2a, 2b) show no noticeable change of the surface morphology of the electrodes between the pristine and cycled samples. In fact, the active material particles appear nearly identical, with the particle size and surface morphology showing no noticeable changes at high magnification. For the LRNM electrodes with 10 wt% $Li_2C_2O_4$ (Fig. 2c), the $Li_2C_2O_4$ is identified as larger, darker particles up of about 5 μm in size compared to the light grey, smaller active material particles which are only up to about 600 nm. The $Li_2C_2O_4$ particles in the pristine electrode (Fig. 2c) are well distributed on the surface and appear to be well mixed with the active material, PVdF binder, and SPC-65 conductive carbon. Figure 2d shows that the $Li_2C_2O_4$ particles decomposed after the first cycle and no remaining $Li_2C_2O_4$ is visible, nor any surface contaminations at elevated magnifications. The porosity of the cycled electrode has clearly increased due to the voids left behind upon decomposition, although this does not have a noticeable effect on the electrochemical performance of the electrodes during the first few cycles, which is consistent with the findings of Solchenbach et al.[29] The EDX maps (Figs. 2c, 2d) of LRNM electrodes with 10 wt% $Li_2C_2O_4$ in both the pristine state and after one cycle confirm that the darker particles in the SEM micrographs consist of $Li_2C_2O_4$. In Fig. 2c, the pristine electrode shows these areas with a purple colour, indicative of a carbon (red) and oxygen (blue) containing composition, which correlates with $Li_2C_2O_4$. The conductive carbon and binder are clearly identified as predominately red areas, composed of pure carbon without the presence of oxygen, and the green area is dominated by transition metals in the LRNM active material. The EDX mappings for the pristine electrode, like the SEM micrographs, reveal a good $Li_2C_2O_4$ distribution on the electrode surface and homogenous mixing with the binder, conductive carbon, and active material, identical to the LRNM cathode with 0 wt% $Li_2C_2O_4$. In Fig. 2d, the cycled electrode shows voids left behind by the decomposed $Li_2C_2O_4$, which increases the surface porosity.

To further elucidate the role of $Li_2C_2O_4$ in the first cycles of the LRNM cathodes, a differential electrochemical mass-spectrometry (DEMS) analysis was carried out on LRNM electrodes with 0 wt% and 10 wt% $Li_2C_2O_4$.[39] Here we followed the approach introduced in the work of Jusys et al.,[31,33] where an Al-sputtered non-porous fluorinated ethylene propylene (FEP) membrane with low permeability for the organic carbonates was employed as a substrate for the LRNM cathode fabrication, which served as interface between the ambient pressure electrolyte and the vacuum system, thus offering a differential detection of the gas evolution rates.[40,41] Under these conditions, the gas evolution rate is directly proportional to the intensity of the mass spectrometer signal.[42]

The decomposition of $Li_2C_2O_4$ as "sacrificial salt" mixed with lithium nickel manganese spinel (LNMO) in full-cells with a silicon/graphite anode was studied previously using a carrier gas driven online electrochemical mass spectrometry (OEMS) approach by Solchenbach et al.[29] The head-space content analysis in these measurements resulted, however, in an integral response, which does not provide rates.

The results of the DEMS measurements performed during the galvanostatic dis-/charge cycles of the respective materials

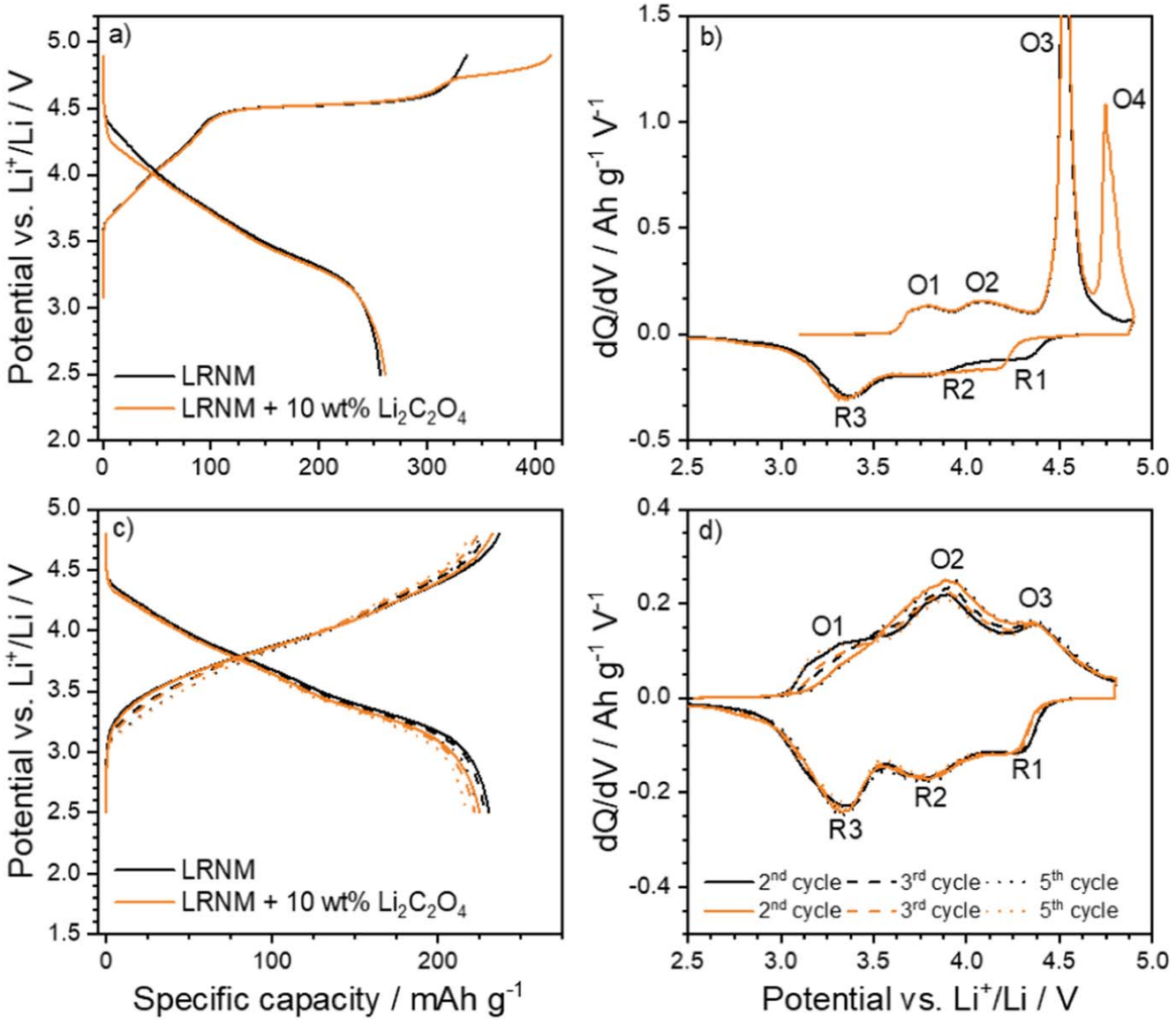

Figure 1. 1st cycle (a) potential profiles and (b) differential capacity plots of LRNM with 0 and 10 wt% $Li_2C_2O_4$. Cycling from 2.5–4.9 V vs Li^+/Li with a C rate of C/20 (at 20 °C). 2nd, 3rd, and 5th cycle (c) potential profiles and (d) differential capacity plots of LRNM with 0 and 10 wt% $Li_2C_2O_4$. Cycling from 2.5–4.8 V vs Li^+/Li with a C rate of C/10 (at 20 °C).

(LRNMO (a) and its mixture with 10 wt% $Li_2C_2O_4$ (b)), are shown in Fig. 3. Charging /discharging was performed at a rate equal to about C/10 in a potential range of 2.5–4.95 V vs Li^+/Li. The potential profiles of the LRNM reference electrode with 0 wt% $Li_2C_2O_4$ and of the LRNM electrode with 10 wt% $Li_2C_2O_4$ are presented in the top panels of Figs. 3a and 3b, respectively. During charge, the potential of the oxalate-free LRNM electrode rapidly increases from ca. 2.9 to ca. 3.7 V, then varies slower to reach ca. 4.53 V, followed by a broad plateau at ca. 4.59 V with a very slow increase of the potential, until again faster increase after reaching ca. 4.6 V up to the upper cut-off voltage of 4.95 V (Fig. 3a). In comparison, for the LRNM electrode with 10 wt% of $Li_2C_2O_4$, the initially rather similar potential trace exhibits a distinct second high-potential plateau at ca. 4.8 V (Fig. 3b). This can be tentatively assigned to the oxidation of $Li_2C_2O_4$, in agreement with a similar second potential plateau reported for a $Li_2C_2O_4$ containing LNMO electrode previously.[29] During discharge, the electrode potential abruptly decreases to ca. 4.5 V, and then slowly decreases to ca. 3.2 V, followed by a faster decrease down to the lower cut-off potential. The subsequent charge cycles do not exhibit the distinct broad potential plateau for the LRNM (Fig. 3a) and the second plateau for the LRNM +10 wt% $Li_2C_2O_4$ (Fig. 3b) that appears during the first charge. Such a potential profile is typical for the layered cathode materials and is usually assigned to the irreversible structural transformations discussed before.

In the simultaneously measured time-resolved gas evolution of the LRNM (Fig. 3a), there is no noticeable ion signal in the first charging cycle until nearly the end of the potential plateau region up to ca. 4.6 V, where O_2 evolution ($m/z = 32$) rapidly increases. This agrees well with previous findings,[15,30,43] and also with the proposal of Wang et al.[37] of a partially irreversible oxidation of lattice oxygen. It is interesting to note that the signal does not appear until the end of the plateau phase at ca. 4.5 V vs Li^+/Li, only slightly before complete de-lithiation of the active material. This provides support to the earlier proposal that oxygen anion oxidation during charge is the last process contributing to the specific capacity of LRNM.[35,37]

Based on previous reports on similar materials, it is assigned to the electrochemical activation of the Li_2MnO_3 domains.[43–45] The maximum O_2 evolution rate is observed at ca. 4.8 V, which was used

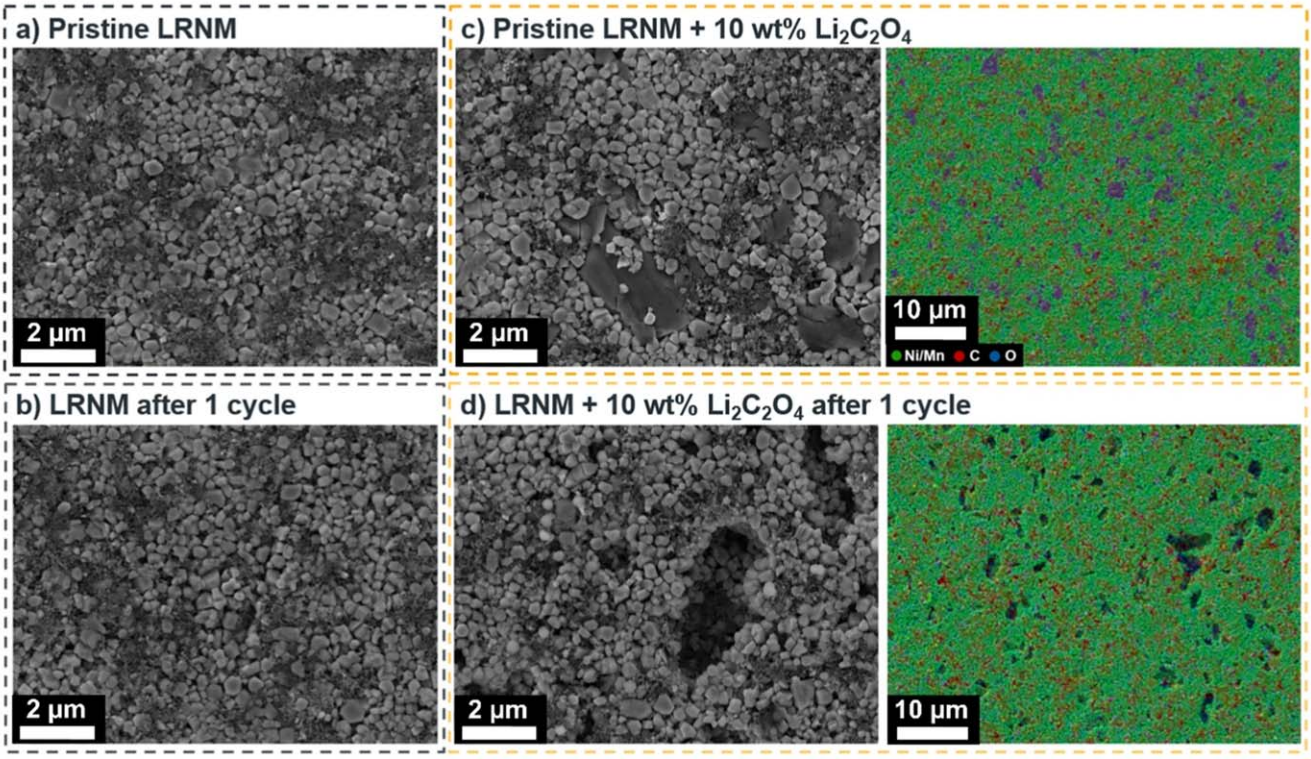

Figure 2. Scanning electron micrographs and EDX maps of LRNM electrodes without additive for (a) a pristine cathode and (b) a cathode after one cycle. SEM image and elemental distribution maps of LRNM electrodes with 10 wt% $Li_2C_2O_4$ for (c) a pristine cathode and (d) a cathode after one cycle. Cycling from 2.5–4.9 V vs Li^+/Li with a C rate of C/20 (at 20 °C).

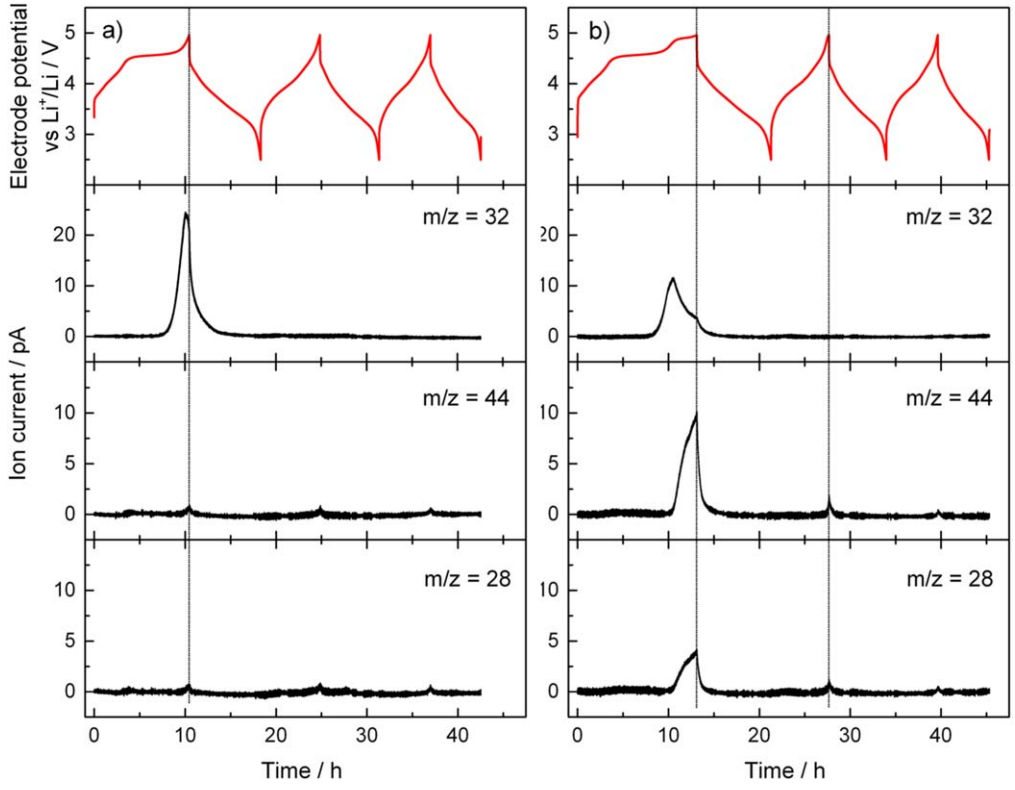

Figure 3. Time dependent differential electrochemical mass spectrometry of gas evolution from LRNM electrodes (a) without the oxalate additive and (b) with 10 wt% $Li_2C_2O_4$. Cycling performed from 2.5–4.95 V vs Li^+/Li and a C rate of C/10 in LP30 as the electrolyte (at 20 °C). The top panels show the galvanostatic potential curves during cycling and the bottom panels show the mass-spectrometer signal currents of selected mass-charge ratios corresponding to O_2 (m/z = 32), CO_2 (m/z = 44), and CO (m/z = 28).

as upper limit in our previous studies,[30,43] followed by a small decay up to the upper potential limit in this work of 4.95 V. This decay in the O_2 formation rate at high potentials may indicate both the depletion of oxygen and/or the possible contribution of some other oxidation process(es), such as transition metal leaching. A careful inspection of the m/z = 44 and m/z = 28 (Fig. 3a) signals, indeed, reveals a small but distinguishable increase when approaching the upper cut-off, which can be attributed to the oxidation of either electrolyte or of electrode components (carbon, binder). The earlier onset of these signals compared to the O_2 evolution at ca. 4.5 V could result, e.g., from the oxidation of surface carbonates.[30] It is important to note, however, that despite the significant O_2 evolution at high potentials, this does not lead to a concomitant increase of CO_2 and CO formation, as could be expected from a possible chemical reaction of oxygen with the organic electrolyte or electrode components. In the subsequent first discharge half-cycle, the O_2 signal subsides quickly as the charging phase completes, and is fully back to background before half-way through the first discharge. This suggests that O_2 evolution stops completely at the end of the charging process. Nonetheless, as discharging proceeds, O_2 is still diffusing out of the electrode, possibly due to the ongoing structural transformations. The following charge-discharge cycles indicate no O_2 release, which is in agreement with the earlier postulated irreversible initial loss of oxygen, whereas a repetitive small increase of m/z = 44 and m/z = 28 still appears at the upper potential limit (Fig. 3a).

Comparing these results to the measurements with LRNM + 10 wt % $Li_2C_2O_4$ in Fig. 3b, the same m/z = 32 ion signal appears again at the end of the LRNM activation plateau at ca. 4.5 V vs Li^+/Li. It is much less intense (12 pA vs 25 pA) for the $Li_2C_2O_4$-containing LRNM electrodes, but nearly twice as broad, taking longer to return to the background level. For the $Li_2C_2O_4$-containing electrodes, the increase of m/z = 32 formation decays at the onset of the second plateau, suggesting that O_2 gas evolution is progressively slowed down with a gradual increase of $Li_2C_2O_4$ oxidation. Due to the constant current during the galvanostatic experiment, the onset of a new electrochemical reaction ($Li_2C_2O_4$ oxidation) competes with the oxidation of oxygen anions to form O_2, which is illustrated by the identical profiles of the mirrored O_2 signal and the simultaneous increase of the CO_2 related signal (Fig. 3b). Hence, the two major electrochemical reactions in this potential range are the oxidation of oxygen anions to O_2 and the oxidation of $Li_2C_2O_4$ to CO_2, with the first setting in positive of ca. 4.6 V and the second at ca. 4.8 V. The latter reaction becomes dominant at higher potentials.

Although the increase of the m/z = 28 ion current with its similar shape as the m/z = 44 transient can be partly assigned to the fragmentation of CO_2 upon electron impact ionization (typically, about 10%[46]), the approximately twice higher m/z = 28 intensity indicates also CO formation. In contrast, the formation of ethene (also at m/z = 28) can be excluded due to the absence of a comparable feature in the simultaneously measured m/z = 27 signal, which is the main fragment of ethene. While the O_2 is released from the LRNM lattice upon oxidation of the oxide anions, the release of CO_2 (and Li^+ ions) results from the oxidation of the $Li_2C_2O_4$ particles, which are physically intermixed with the LRNM. The latter reaction leads to the formation of the empty voids observed in the SEM images (Fig. 2). On the other hand, such an "open" morphology can facilitate the release of O_2 from the LRNM + 10 wt % $Li_2C_2O_4$, as evidenced from the faster m/z = 32 ion current decrease in the latter case (Fig. 3b) compared to LRNM (Fig. 3a). As mentioned above, CO is in principle together with CO_2 a product of EC and DMC decomposition at high potentials, and due to the $Li_2C_2O_4$ decomposition plateau the cell remains at elevated potential for longer time than the oxalate-free LRNM cell (about 2 h at C/10). However, these signals are relatively weak in Fig. 3a. Hence, it is likely that the vast majority of these signals in Fig. 3b is due to $Li_2C_2O_4$ oxidation and not caused by solvent decomposition. Another tentative explanation for the stronger than expected CO signal is that the $Li_2C_2O_4$ oxidation products are not only CO_2, but also CO and O_2. More importantly though, the MS scans obtained during the second and third charge cycle are almost identical to those of LRNM without oxalate, whereas somewhat higher CO_2 and CO signals at the positive cut-off potential during the second charging of the LRNM + 10 wt% $Li_2C_2O_4$ electrode could result from traces of superficial lithium carbonate species formed in the preceding first charge or oxalate residues. This indicates that $Li_2C_2O_4$ decomposition is, indeed, almost fully completed after the first cycle and does not lead to the formation and release of a significant amount of additional side products upon the subsequent cycles. This latter fact is of great practical importance, as it means that continuous gassing, which has to be strictly avoided, is not an issue after the initial formation cycle. Continuous gassing must be avoided because when the scale-up and manufacturing of these cells is considered then once the cell is closed and sealed then gassing would result in unwanted pressure build-up and potential venting. If gassing is completed in the initial formation cycle then this is an ultimate positive for production consideration because then the cell can be closed after the formation, called open formation, which is already a proven method.

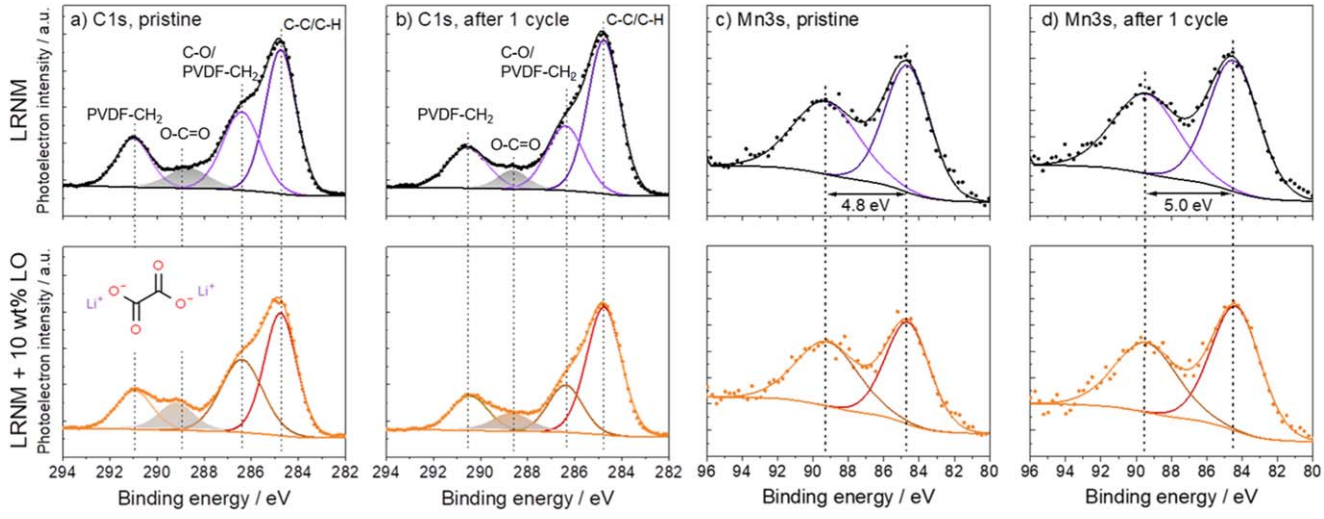

Figure 4. XPS spectra recorded on LRNM electrodes without (top) and with 10 wt% $Li_2C_2O_4$ (bottom) of pristine (a), (c) and cycled electrodes (b), (d) after one cycle between 2.0–4.9 V vs Li^+/Li at a C rate of C/20 (at 20 °C) in the C1s and Mn3s regions. The shaded area the C1s region marks the fit corresponding to O–C=O species. The dashed lines in the Mn3s region mark the positions of the maxima of the two fitted Mn3s peaks.

The release of possibly reactive gases within the cell and the slight alteration of the potential profiles during the first discharge cycle (Fig. 1) demand an in-depth investigation of the impact of the $Li_2C_2O_4$ decomposition products on the surface properties of the electrodes. For this purpose, a surface chemical characterization of the LRNM electrodes was performed using XPS. The XPS spectra in Fig. 4 show significant changes of the surface composition after one charge/discharge cycle, as well as differences between LRNM electrodes with 0 wt% and 10 wt% $Li_2C_2O_4$.

The C1s spectra shown in Figs. 4a, 4b display four distinct peaks. The first feature (at 284.8 eV) can be assigned to C–C/C–H species, the second (at 286.4 eV) is a superposition of intensities related to C–O groups and the CH_2 groups of the PVdF binder, the third peak (at 288.6 eV) can be attributed to carboxyl groups (O–C=O), while the CF_2 groups of PVdF binder lead to the last peak at 291.0 eV. We are mainly interested in the third feature, which includes besides, e. g., surface carbonates also the signal of the $Li_2C_2O_4$ groups. Indeed, this peak has a slightly higher intensity for the uncycled electrode with $Li_2C_2O_4$ addition (bottom panel of Fig. 4a) compared to the other three samples and is shifted to a slightly higher binding energy close to 289 eV. These differences are related to the presence/absence of the $Li_2C_2O_4$ compound. After the first cycle (bottom panel of Fig. 4b), its peak intensity is reduced due to the oxidation of $Li_2C_2O_4$ to gaseous CO_2. The oxidation to CO_2 is the desired reaction pathway as the alternative would be the formation of transition metal carbonate contaminates, which would show a more intense peak at around 290.5 eV. Based on the comparison of the bottom panel of Fig. 4b with the upper one from the cycled sample without $Li_2C_2O_4$, there are no major contributions from such carbonates.[47,48]

Another possible hint for the presence or absence of undesirable reaction products might be derived from the Mn oxidation state. For this purpose, XPS detail spectra in the Mn3s region were recorded on the pristine and cycled electrodes (Figs. 4c, 4d). It was shown earlier that the degree of the multiplet splitting of this peak can be a diagnostic tool for the Mn oxidation state. A splitting of ~6 eV was found for Mn^{2+}, decreasing to ~5.5 eV for Mn^{3+} and ~4.8 eV for Mn^{4+} for oxides with other oxidation states (from MnO to MnO_2).[49] In our case, a peak splitting of 4.8 eV is observed for both pristine samples (without and with 10 wt% $Li_2C_2O_4$), which changes to 5.0 eV for both cycled samples. The results indicate that the Mn oxidation state is, as expected, in both cases Mn^{4+} for the pristine electrodes. The slightly enlarged peak splitting of the cycled samples points to the presence of some Mn^{3+} in the cycled samples. More precisely, the change in the Mn oxidation state from the pristine to the cycled electrodes can be attributed to a partial reduction of the Mn^{4+} in the MnO_2 nano-domains on the surface to Mn^{3+} in $LiMnO_2$ when discharging LRMN below 3.6 V vs Li^+/Li to $LiMnO_2{\cdot}LiMO_2$, while the Mn^{4+} in the $LiMO_2$ domains should remain largely unchanged along with the bulk material.[37] Importantly, this behaviour is exactly the same for both electrode types, which indicates that no further Mn reduction and $MnCO_3$ formation occurs in the presence of the $Li_2C_2O_4$ (pristine, Fig. 4c) or due to the release of CO_2 during cycling (after 1 cycle, Fig. 4d).

Figure 5 shows the XPS detail spectra of the O1s, F1s, and P2p regions for the cycled electrodes (without and with 10 wt% $Li_2C_2O_4$). The O1s peak at 529.8 eV can be ascribed to the bulk transition-metal oxide (M–O).[35] The peak at 532.0 eV is characteristic for C=O bonds in carbonate species. The peak at 533.3 eV is assigned to C–O bonds. The M–O peak for the sample without $Li_2C_2O_4$ is much more intense than the one for the sample with 10 wt% $Li_2C_2O_4$. In contrast, the intensity of C–O and C=O peaks is not so different for the two electrodes. The smallest intensity of the M–O peak points to a thicker cover layer on the LRNM particles with other surface species for the electrode with 10 wt% $Li_2C_2O_4$.

This interpretation is supported by the F1s spectra, which show peaks related to PVdF (CF_2) at 688.1 eV, to intermediate decomposition products ($Li_xPO_yF_z$) of the electrolyte salt at 687.2 eV, and to lithium fluoride (LiF) at 685.0 eV. LiF is a key component of the cathode-electrolyte interphase (CEI) layer formed as a result of the decomposition of $LiPF_6$, similar to the process within the SEI.[35,50] The comparison of the spectra for the two electrodes shows a smaller intensity of the PVdF signal, but more intensity for the $Li_xPO_yF_z$ and LiF peaks for the sample containing 10 wt% $Li_2C_2O_4$. This has not been shown in previous literature and corroborates the conclusion that the CEI layer on the LRNM electrode with 10 wt% $Li_2C_2O_4$ is thicker and contains a higher concentration of the final product LiF.[35,51] It could also mean that the reactions forming the CEI are proceeding through the intermediate stages at a faster rate and that this is developing faster during the first cycle. Solchenbach et al.[29] reasoned that CO_2 from the decomposition of $Li_2C_2O_4$ is beneficial in forming a more effective SEI layer on a Si–C anode, which was beneficial in terms or cycling performance. It is possible that this effect is similar on the LRNM cathodes, leading to a clear difference in CEI thickness and composition between the cathodes with and without the $Li_2C_2O_4$ additive. However, it is also possible that the prolonged duration of the cathode cycling at high potentials due to the added capacity of $Li_2C_2O_4$ decomposition at 4.7 V vs Li^+/Li is facilitating more electrolyte decomposition and thicker CEI growth.

In the next step, the impact of the oxalate on the electrochemical performance was assessed in half-cells using Li metal as the counter electrode (Fig. S1). LRNM cathodes with 0, 5, and 10 wt% $Li_2C_2O_4$ were cycled with increasing C rates from C/10 up to 10 C within the potential range of 2.5–4.8 V vs Li^+/Li after an activation cycle at C/20. After the rate performance tests, the cells were cycled further at a C rate of 1 C for 200 cycles. After completing the 200 cycles at 1 C, the LRNM cathode with 5 wt% $Li_2C_2O_4$ had the best average capacity retention (89%), whereas those with 0 and 10 wt% showed capacity retentions of 87.3% and 86%, respectively. In order to demonstrate the clear presence of lithium plating on the graphite anode, the subsequent measurements were performed using electrodes with 10 wt% $Li_2C_2O_4$. The lithium plating is seen in the circled area of Fig. 6b and is indicate by an increase of specific capacity at a constant 0.0 V on the anode. Overall, the above results confirm the absence of any significant negative impact of the presence and decomposition of $Li_2C_2O_4$ on the electrochemical performance of LRNM cathodes, while it is adding to the initial charge capacity. The $Li_2C_2O_4$ is entirely decomposed during the first charge and the CO_2 gas evolution is limited to the very first cycle.

Finally, graphite||LRNM full-cells and graphite||LRNM with 10 wt% $Li_2C_2O_4$ full-cells were subjected to rate capability tests and subsequent constant current cycling in order to compare the impact of the $Li_2C_2O_4$ on full-cells with a graphite anode. The individual potential profiles for the positive and negative electrodes of two representative cells during the initial activation cycle (2.0–4.9 V cell voltage at a C rate of C/10) are shown in Figs. 6a, 6b. The upper cut-off voltage was chosen in order to achieve full decomposition of lithium oxalate. The first cycle shows that the cell without $Li_2C_2O_4$ was precisely balanced with full lithiation of the graphite, while for the cell with $Li_2C_2O_4$, as expected, additional lithium was plated initially on the graphite anode after the complete lithiation, with the excess lithium provided from the decomposition of $Li_2C_2O_4$ in the cathode. This extra lithium was released upon discharge from the anode again and, as a consequence, the graphite was not yet fully de-lithiated at the end of discharge in this case, providing an internal lithium reservoir for the long-term cycling. Remarkably, this also increased the initial reversible capacity of the cells from 248 to 258 mAh g^{-1} when comparing cells without and with the $Li_2C_2O_4$ additive. Rate tests were then performed as shown with the upper and lower voltage cut-offs being chosen to optimize the capacity. After the initial cycle the voltage range is reduced to 2.0 to 4.75 V, at C/2 the upper cut-off voltage is increased to 4.8 V and when 1 C is reached then additionally the lower voltage cut-off is lowered to 1.8 V. The graphite||LRNM cells without $Li_2C_2O_4$ performed on average slightly better at lower C rates, but lost slightly more in capacity for increasing C rates, nearly approaching the same value (164 mAh g^{-1}) as those with $Li_2C_2O_4$ (160 mAh g^{-1}) at 2 C (Fig. 6c).

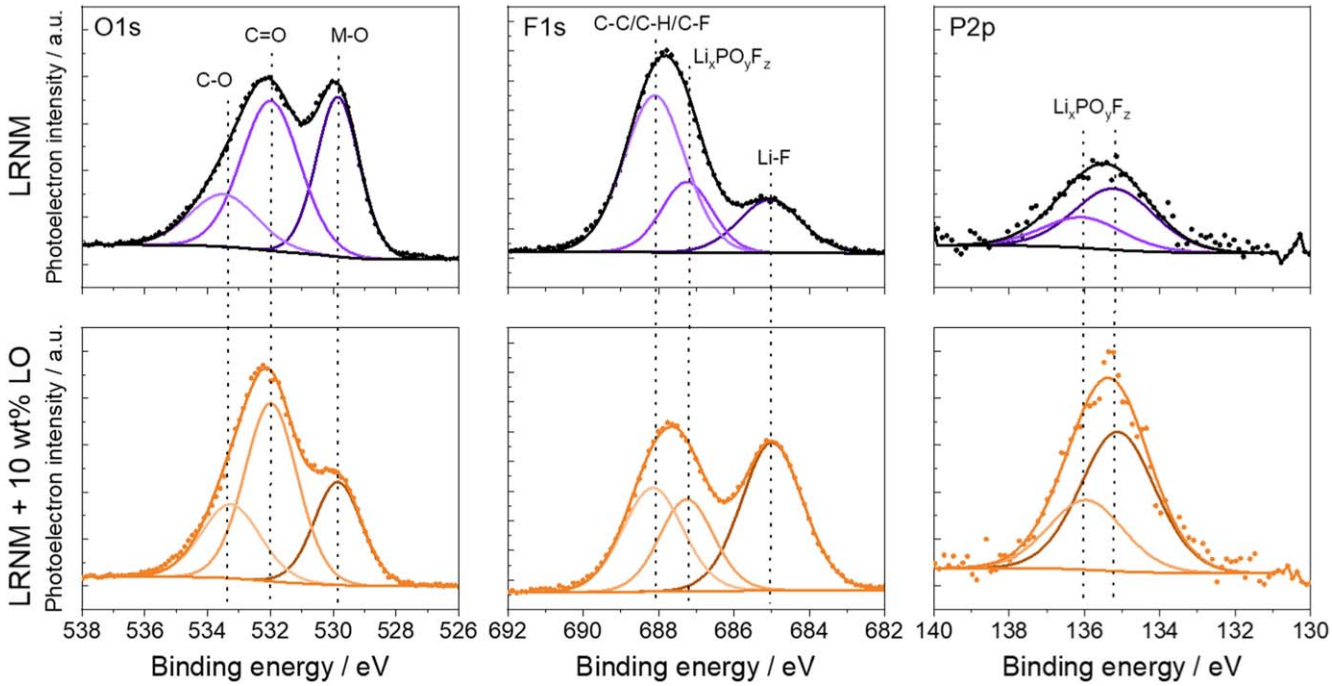

Figure 5. XPS detail spectra recorded in the O1s, F1s, and P2p regions from LRNM electrodes without (top) and with 10 wt% $Li_2C_2O_4$ (bottom) after one cycle between 2.0–4.9 V vs Li^+/Li at a C rate of C/20 (at 20 °C).

After completion of the rate performance tests, the cells were subjected to cycling at 1 C between 2.0 and 4.8 V (Fig. 6c). Upon cycling, the available lithium inventory is expected to remain elevated in pre-lithiated cells. This concept has also been successfully demonstrated by Solchenbach et al.[29] in their experiments with graphite||LRNM cells in 1 M $LiPF_6$ in EC:EMC (3:7, w:w) as the electrolyte. Our results are very promising with regard to the Coulombic efficiency (CE) and cycle life. The average CE for the LRNM + 10 wt% $Li_2C_2O_4$ cells after 400 cycles at 1 C is 99.92% compared to 99.78% for LRNM without $Li_2C_2O_4$. The cycle life of the LRNM + 10 wt% $Li_2C_2O_4$ cells was far greater than that of the control cells, even completing the full 1,000 cycle test. Differently, the best performing LRNM cell without $Li_2C_2O_4$ dropped off dramatically after about 475 cycles. Hence, the addition of 10 wt% $Li_2C_2O_4$ results in a doubled cycle life.

To gain a deeper understanding of the initial cycling behaviour and the influence of the pre-lithiation in a full-cell configuration, single-layer pouch cells were assembled using spherically shaped and scalable LRNM material of similar composition in the cathode against graphite anodes. 5 or 10 wt% $Li_2C_2O_4$ were added to the cathode slurry during the mixing process. Figure 7 compares the morphology of ball-milled electrodes (LRNM + 10 wt% $Li_2C_2O_4$) and electrodes with spherical LRNM + 10 wt% $Li_2C_2O_4$ before and after the formation cycles. As already indicated in the top-view SEM images of the ball-milled LRNM + 10 wt% $Li_2C_2O_4$ electrodes in Fig. 2, the dark grey particles, which were assigned to the $Li_2C_2O_4$, were homogenously distributed in the electrode. Furthermore, the cross-section indicated an increase of the porosity after the formation cycles. For the electrodes with spherical LRNM + 10 wt% $Li_2C_2O_4$, the oxalate particles were also homogeneously distributed in the uncycled electrode. The larger size of the $Li_2C_2O_4$ particles can be explained by the omitted and not necessary ball-milling step during the slurry preparation (see Experimental). Raman microscopy was used to corroborate the assignment of $Li_2C_2O_4$ particles in the electrode (Figs. 7c, 7f). The spectra of the spherical LRNM particles (orange) showed vibrational bands at 431, 494, and 606 cm^{-1}, which are characteristic of LRNM as discussed in our previous work.[52] Particles with irregular morphology (coloured in blue) showed very strong Raman vibration bands at 910, 1488 and 1649 cm^{-1} and can be assigned to $Li_2C_2O_4$.[53,54] These measurements clearly proved the presence of $Li_2C_2O_4$ in the electrodes and underlined the assignment of the dark grey spots in the SEM images with the $Li_2C_2O_4$ particles by the correlation of EDX mapping and SEM imaging in Fig. 2c. In Fig. 7e, irregularly shaped cavities are observed after formation of the electrode similar to the ball-milled electrodes, which indicates the complete decomposition of the oxalate and the formation of additional porosity within the electrode. Raman microscopy was not able to detect any $Li_2C_2O_4$ signal in the cavities.

The electrochemical decomposition of $Li_2C_2O_4$ during the first cycle in the pouch cell LRNM cathodes with spherical material differed from that in the ball-milled material in the small circular electrodes. Because a complete decomposition during the first cycle was not possible at room temperature due to larger $Li_2C_2O_4$ particle size, the formation of the pouch-cells was conducted at an elevated temperature of 40 °C to speed up the reaction kinetics. At this temperature, the shape of the pouch-cell potential curves was similar to that of the LRNM cells with irregular particle morphology (Figs. 8a, S2). Depending on the amount of additional $Li_2C_2O_4$, the plateau at approximately 4.7 V was elongated. As a result, the irreversible capacity loss in the first cycle increased. The effect of the pre-lithiation was also observed during the post-mortem analysis of the cells, where an increase of the blueish colour of the lithiated graphite (see Fig. S3) in the anode sheets is observed. As expected, during the formation cycle a large amount of gas was released, which is evident from the expansion of the gasbags (Fig. 8c). To quantify the volume of the evolved gas, the buoyant force of the cells was determined before and after the formation cycles using the Archimedes principle[32] (Fig. 8b). Electrodes without additional $Li_2C_2O_4$ released approximately 7 ml g^{-1} of gas during the formation cycles due to O_2 evolution and possible side-reactions, e.g., electrolyte decomposition. With the addition of $Li_2C_2O_4$, this value increased up to approximately 40 ml g^{-1} for an electrode with 10 wt % $Li_2C_2O_4$. Figure 8b also compares the theoretical gas evolution volumes, assuming a complete $Li_2C_2O_4$ decomposition, with the experimental data. At first, the gas volumes for the cells with $Li_2C_2O_4$ seem to differ strongly from the theoretical values. However, it is very important to consider other reactions during the formation cycles that lead to gas evolution. When adding the

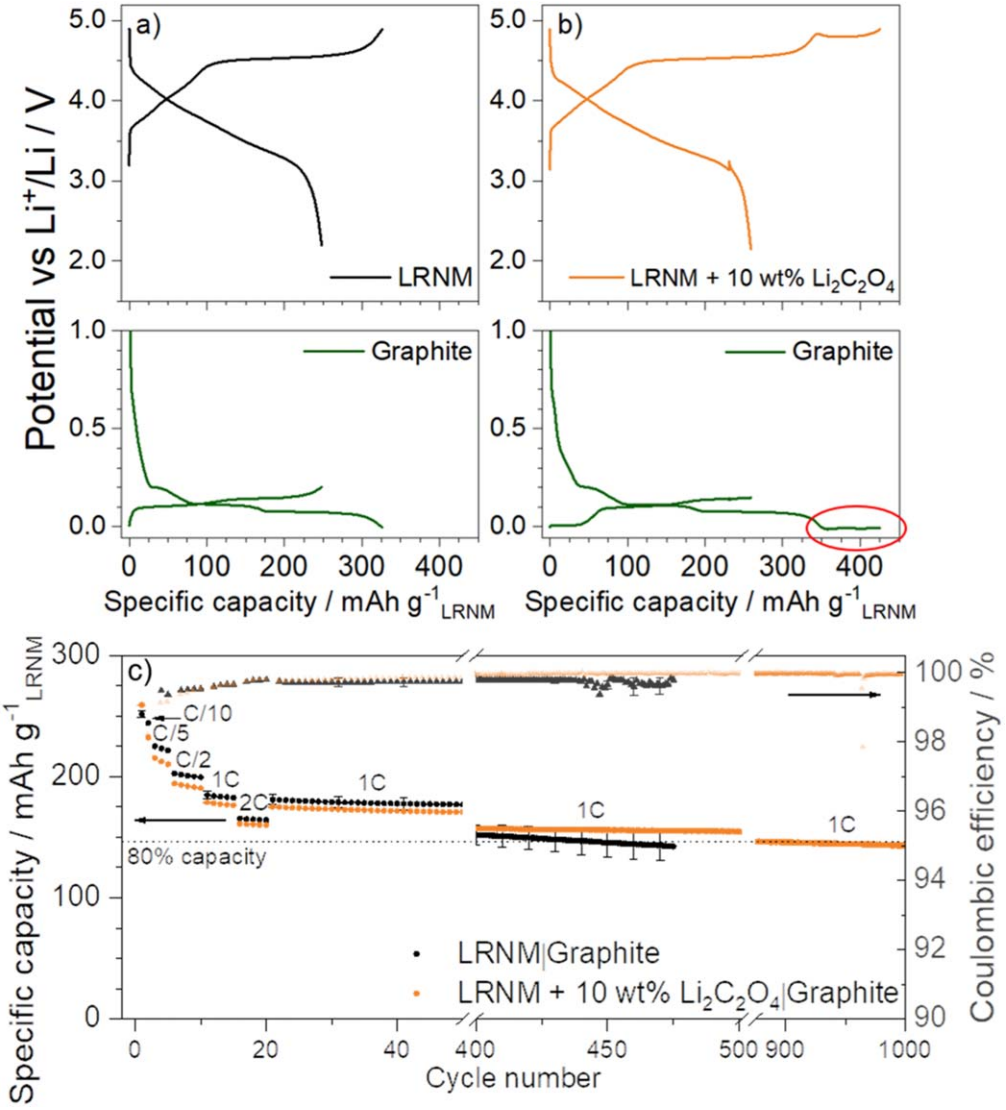

Figure 6. Potential profiles of the first cycle of (a) graphite||LRNM and (b) graphite||LRNM full-cells with 10 wt% $Li_2C_2O_4$ cells showing the positive (top) and negative (bottom) electrode potentials individually. (c) Rate capability and long-term cycling performance. The cells were first cycled at increasing C rates from C/10 to 2C, then at 1 C for 1,000 cycles or until failure. The 1 C cycling was performed at 20 °C and with 1.8 and 4.8 V as cut-off voltages.

volume of gas detected in the oxalate-free cell to the theoretical value, the experimental result for LRNM + 5 wt% $Li_2C_2O_4$ is very close to the theoretical value. For LRNM + 10 wt% $Li_2C_2O_4$, there is still a gap between the theoretical and experimental value. This could be the result of a larger amount of side-reaction products due to the increased time that the cell spent in the high-voltage region in order to decompose the $Li_2C_2O_4$.

Additionally, the pore size distribution (PSD) of the electrodes after the formation cycle was investigated using Mercury intrusion porosimetry (Fig. 8d). All electrodes were calendared to the same density (1.6 g cm^{-3}) before cell assembly. In general, two different maxima were observed for the PSD in the measured pore size range, with the first maximum between 0.06 and 0.09 μm and the second maximum between 0.3 and 0.4 μm. Larger pore sizes (>10 μm) were not considered in this discussion due to the absence of larger pores in the SEM cross-sections. When comparing the peak positions and the intensity ratio of both peaks, a strong intensity change of the second peak was observed. Whereas the second peak was only visible as a shoulder for the oxalate-free electrode, a pronounced peak appeared for the $Li_2C_2O_4$-containing composite. Simultaneously, the peak at lower pore sizes decreased and its maximum shifted to lower values. Both observations confirm that the decomposition of $Li_2C_2O_4$ resulted in new pores during the formation cycles, as also supported by the SEM analysis of the electrodes. Therefore, $Li_2C_2O_4$ can be used for pre-lithiation of the graphite anode and simultaneously as an operando pore-forming agent on the cathode side.

It has been clearly demonstrated that one of the major challenges with nanostructured Si anodes is the high first-cycle lithium consumption due to their high surface area (and the use of Si in general), which results in significant lithium consumption during the formation of the SEI layer.[55,56] The comparison of different electrolytes (LP30, LP30 + 3 wt% FEC or VC) with the a-Si/CuSi NW anode showed that the LP30 + 3 wt% FEC has the lowest irreversible capacity loss, and the best cycling behaviour for half-cells during rate tests and prolonged cycling (Fig. S4). Hence, LRNM with 3 wt% $Li_2C_2O_4$ was paired in the next step with an a-Si/CuSi NW anode and compared to an oxalate-free cell using LP30 + 3 wt% FEC as the electrolyte. A calculation was carried out to determine the optimal weight percent of additive in the cathode to be in coordination with the silicon loading of 0.15 $mgcm^{-2}$ of the anode. The a-Si/CuSi NW||LRNM lithium-ion cells were electrochemically tested using the same procedure as for the graphite|| LRNM cells to analyse the rate and long-term cycling performance. The potential profiles of the positive and negative electrodes of the

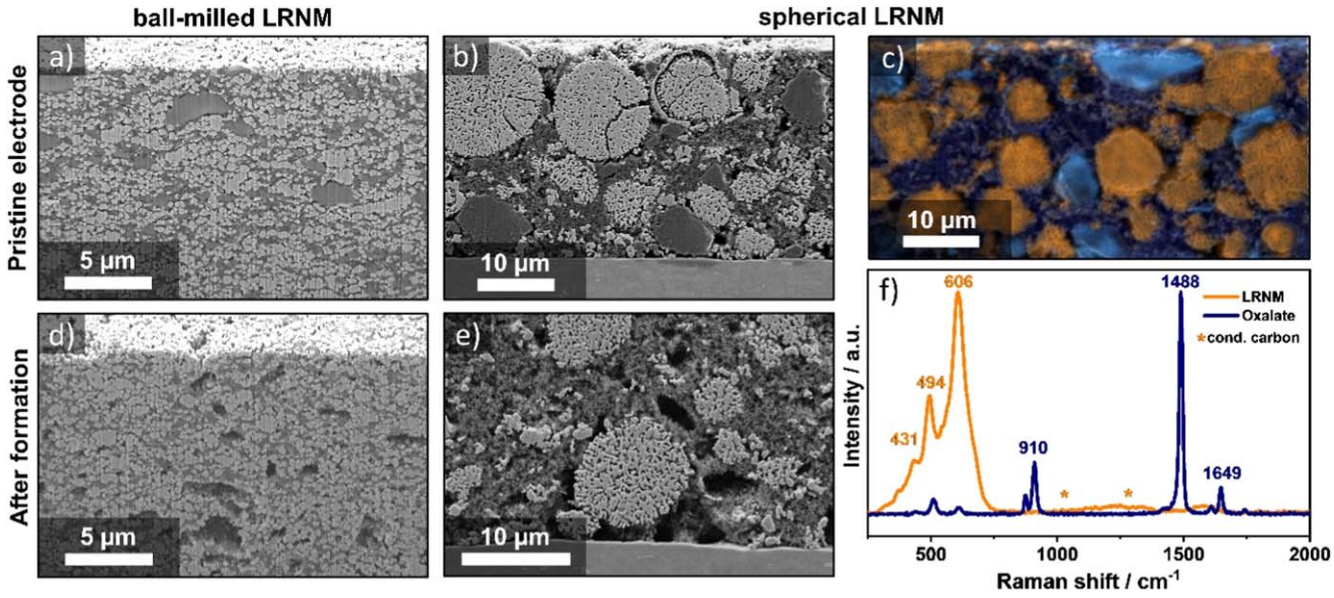

Figure 7. Comparison of SEM electrode cross-sections with (a), (d) ball-milled LRNM and (b), (e) scalable spherical LRNM material both with 10 wt% $Li_2C_2O_4$. (c), (f) Raman spectroscopy results for an electrode cross-section with spherical LRNM particles (orange) and $Li_2C_2O_4$ particles (blue).

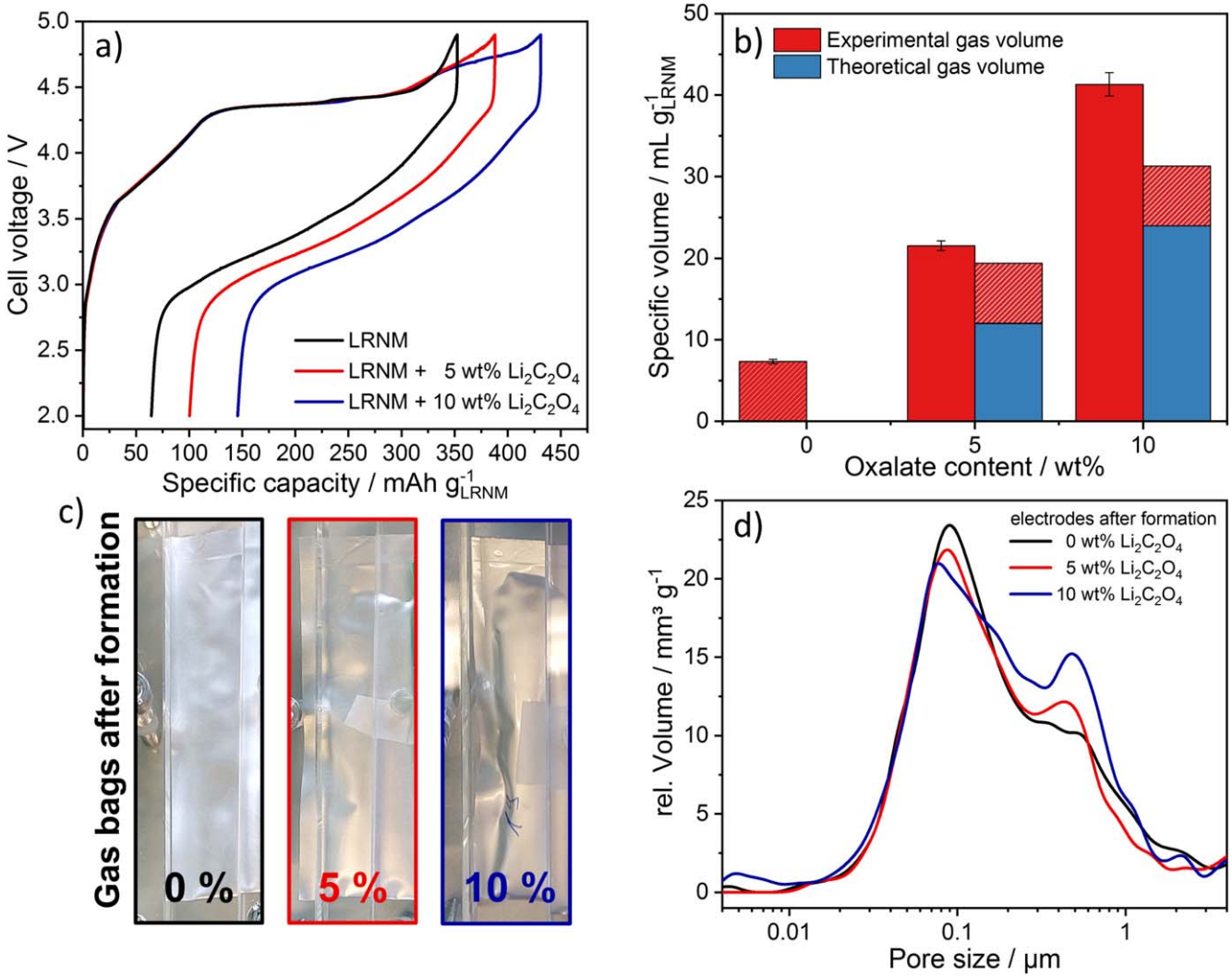

Figure 8. (a) Voltage profiles of the 1st cycle of scalable spherical LRNM electrodes without $Li_2C_2O_4$ (black), with 5 wt% $Li_2C_2O_4$ (red), and with 10 wt% $Li_2C_2O_4$ (blue) at 40 °C. (b) Comparison of the measured gas volumes after the formation (red) and theoretically expected values (blue, $Li_2C_2O_4$ decomposition), considering the gas evolution from other processes than $Li_2C_2O_4$ decomposition (red-and-white striped). (c) Gas bags of the pouch-cells after the formation. (d) Pore size distribution of scalable spherical LRNM electrodes without $Li_2C_2O_4$, with 5 wt% $Li_2C_2O_4$, and with 10 wt% $Li_2C_2O_4$ after formation.

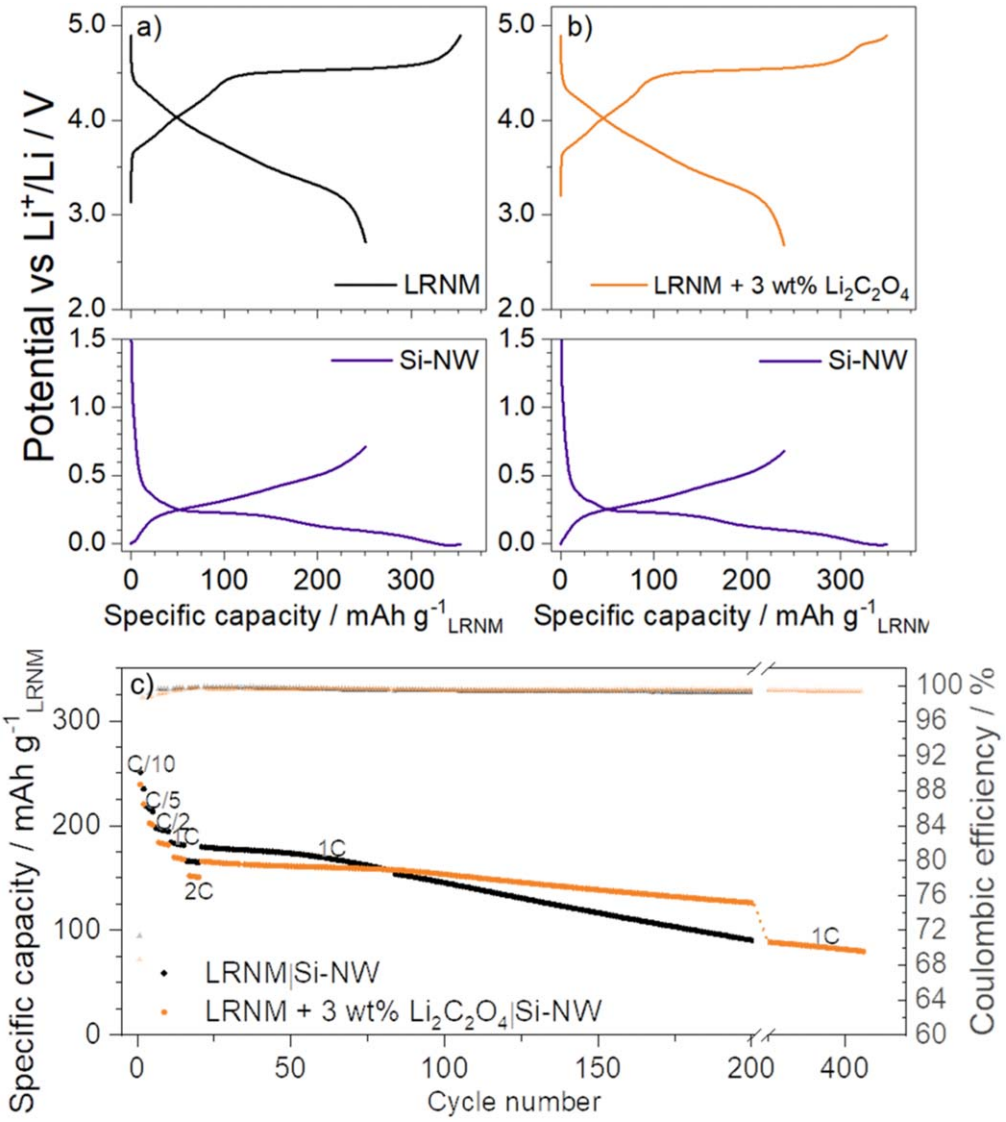

Figure 9. First cycle potential profiles of (a) a-Si/CuSi NW||LRNM full-cells and (b) a-Si/CuSi NW||LRNM with 3 wt% $Li_2C_2O_4$ full-cells with LP30 + 3 wt% FEC as electrolyte during cycling the cell voltage range from 2.0 to 4.9 V with a C rate of C/10 in three-electrode cells (at 20 °C). (c) Rate capability and long-term cycling test of a-Si/CuSi NW||LRNM lithium-ion cells with LRNM cathodes containing 0 and 3 wt% $Li_2C_2O_4$ with increasing C rates from C/10 to 2C, before constant current cycling at 1 C until 80% of the initial capacity (20 °C). The cut-off voltages were 2.0–4.75 V at C/10 and C/5, 2.0–4.8 V at C/2, and 1.8–4.8 V at 1 C and 2 C.

two cells during the first cycle (4.9 V cell voltage at a C rate of C/10) are shown in Figs. 9a, 9b. The initial charge capacity of the oxalate-free cell was 353 mAh g^{-1}, compared to 349 mAh g^{-1} for the 3 wt% $Li_2C_2O_4$ containing cell. The reversible capacities were 239 and 251 mAh g^{-1}, respectively. Although these results are quite comparable, it was expected that the cell with $Li_2C_2O_4$ should show a slightly higher capacity for the first charge and then return to 250 mAh g^{-1} for the discharge. The likely explanation for this discrepancy is that the cathode becomes more polarized due to a slight overestimation of the active material mass and, thus, a higher specific current was applied. The cathode potentials at the end of the first discharge support this idea: 2.68 V vs Li^+/Li (LRNM + 3 wt% $Li_2C_2O_4$) and 2.71 V vs Li^+/Li (LRNM). The first charge capacities are higher compared to the Li-metal||LRNM cells (350 and 337 mAh g^{-1}) due to the presence of the FEC additive.

After the successful activation cycle, the cells were cycled up to a C-rate of 2 C. The difference in discharge capacity of 14 mAh g^{-1} was maintained at each rate (Fig. 9c), conclusively showing that the addition of $Li_2C_2O_4$ into the cathode has no adverse effect on the rate performance when paired with a-Si/CuSi NW anodes. This becomes more interesting when comparing to the rate performance of the Li-metal||LRNM and Li-metal||LRNM cells. In the Li-metal|| LRNM cells, the difference in capacity widens between the cells with and without oxalate as the rate is increased. The opposite is true for the graphite||LRNM cells, where the difference becomes smaller at increasing C rates. The observation that these two effects essentially balance out with the a-Si/CuSi NW anodes provides insights into the development of the SEI. Likely, less Li_2CO_3 is able to form in the SEI due to the fewer amount of carbon species which are more abundant in the graphite.[57] As a result, the SEI growth is neither hindering nor enabling better rate performance in contrast to the graphite||LRNM cells.

Different to the rate performance test, there is an obvious difference in cycling performance between the a-Si/CuSi NW|| LRNM cells with and without $Li_2C_2O_4$ (Fig. 9c). At the start of the cycling test, the a-Si/CuSi NW||LRNM cell with 3 wt% $Li_2C_2O_4$ had a discharge capacity of 166 mAh g^{-1} and 99.63% CE. After 200 cycles at 1 C (1.8–4.8 V) this decreased to 122 mAh g^{-1} and 99.49% CE. The a-Si/CuSi NW||LRNM cell without oxalate started cycling at 180 mAh g^{-1} and 99.77% CE, but decreased to 80 mAh g^{-1} and

99.18% CE after 200 cycles. Hence, the cycling performance for the $Li_2C_2O_4$ containing cell is far superior to the cell without oxalate, with a capacity retention of 74% vs only 44% after 200 cycles. The cell with $Li_2C_2O_4$ continued to cycle to 400 cycles with the CE only reducing to 99.31% with 48% capacity retention, once again doubling the cycle life as observed for the graphite||LRNM cells.

Conclusions

LRNM electrodes without and with adding $Li_2C_2O_4$ were made and electrochemically tested via galvanostatic techniques vs lithium metal and it was found that $Li_2C_2O_4$ has no detrimental effects on the cathode active material in both rate and cycling tests. Additionally, physicochemical characterization using DEMS, FIB-SEM, SEM, Raman and XPS clearly proved that the $Li_2C_2O_4$ decomposition is almost completed after the first cycle and does not lead to the formation of additional side products upon subsequent cycles. Furthermore, the gas evolved during the initial formation cycle was quantified and differences in the cathode porosity were identified by the investigation of pouch cells. Together with the electrochemical characterization, these results suggest that the presence of $Li_2C_2O_4$ promotes an effective SEI/CEI growth during the first cycle, which is then expected to contribute to a better cycling stability and operando formation of internal porosity.

Oxalate-free LRNM electrodes and LRNM electrodes with 10 wt % $Li_2C_2O_4$ were assembled in full lithium-ion cells with graphite anodes and tested once again using galvanostatic rate and cycling procedures. This could prove that the oxidation of $Li_2C_2O_4$ in the LRNM has no appreciably detrimental effects on the graphite|| LRNM cell performance for C rates up to 2C. Indeed, it has an added benefit of SEI stabilization via CO_2 absorption into the electrolyte for graphite anodes along with providing an excess lithium reservoir. Overall, this enabled the LRNM electrodes with oxalate to outperform the oxalate-free electrodes by doubling the cycle life.

Following this, a similar analysis was performed with oxalate-free and 3 wt% $Li_2C_2O_4$-containing LRNM electrodes paired with a-Si/CuSi NW anodes. The oxalate containing cells demonstrated the effectiveness of the cathode pre-lithiation method in providing a lithium reservoir to compensate the initial SEI growth and nearly doubled the cycle life from 220 to 400 cycles.

Acknowledgments

This project has received funding from the European Union within the Horizon 2020 research and innovation programme under grant agreement No 814464 (Si-Drive), from the German Federal Ministry of Education and Research (BMBF) in the frame of the ExcellBattUlm project (03XP0257D and 03XP0257C), and from the Helmholtz Association. This work contributes to the research performed at CELEST (Center for Electrochemical Energy Storage Ulm-Karlsruhe). Moreover, the authors would like to thank W. Weirather for his support during upscaling of the LRNM material, and G. Arnold for ICP measurements (both ZSW).

ORCID

Florian Klein https://orcid.org/0000-0002-8768-0111
R. Jürgen Behm https://orcid.org/0000-0002-7565-0628
Dominic Bresser https://orcid.org/0000-0001-6429-6048
Peter Axmann https://orcid.org/0000-0003-0274-1796
Stefano Passerini https://orcid.org/0000-0002-6606-5304

References

1. M. Li, J. Lu, Z. Chen, and K. Amine, "30 years of lithium-ion batteries." *Adv. Mater.*, **30**, 1 (2018).
2. D. Bresser, K. Hosoi, D. Howell, H. Li, H. Zeisel, K. Amine, and S. Passerini, "Perspectives of automotive battery R&D in China, Germany, Japan, and the USA." *J. Power Sources*, **382**, 176 (2018) .
3. X. Zeng, M. Li, D. Abd El-Hady, W. Alshitari, A. S. Al-Bogami, J. Lu, and K. Amine, "Commercialization of lithium battery technologies for electric vehicles." *Adv. Energy Mater.*, **9**, 1 (2019).
4. G. G. Eshetu, H. Zhang, X. Judez, H. Adenusi, M. Armand, S. Passerini, and E. Figgemeier, "Production of high-energy Li-ion batteries comprising silicon-containing anodes and insertion-type cathodes." *Nat. Commun.*, **12**, 1 (2021).
5. J. Wang, T. Xu, X. Huang, H. Li, and T. Ma, "Recent progress of silicon composites as anode materials for secondary batteries." *RSC Adv.*, **6**, 87778 (2016).
6. C. K. Chan, H. Peng, G. Liu, K. McIlwrath, X. F. Zhang, R. A. Huggins, and Y. Cui, "High-performance lithium battery anodes using silicon nanowires." *Nat. Nanotechnol.*, **3**, 31 (2008).
7. C. K. Chan, X. F. Zhang, and Y. Cui, "High capacity Li ion battery anodes using Ge nanowires." *Nano Lett.*, **8**, 307 (2008).
8. L. F. Cui, R. Ruffo, C. K. Chan, H. Peng, and Y. Cui, "Crystalline-amorphous core–shell silicon nanowires for high capacity and high current battery electrodes." *Nano Lett.*, **9**, 491 (2009).
9. M. N. Obrovac and L. Christensen, "Structural changes in silicon anodes during lithium insertion/extraction." *Electrochem. Solid-State Lett.*, **7**, 5 (2004).
10. K. Stokes, H. Geaney, M. Sheehan, D. Borsa, and K. M. Ryan, "Copper silicide nanowires as hosts for amorphous Si deposition as a route to produce high capacity lithium-ion battery anodes." *Nano Lett.*, **19**, 8829 (2019).
11. T. Li, X. Z. Yuan, L. Zhang, D. Song, K. Shi, and C. Bock, "Degradation mechanisms and mitigation strategies of nickel-rich NMC-based lithium-ion batteries." *Springer Singapore*, **3**, 43 (2020).
12. P. Rozier and J. M. Tarascon, "Review—Li-rich layered oxide cathodes for next-generation Li-ion batteries: chances and challenges." *J. Electrochem. Soc.*, **162**, A2490 (2015).
13. F. Wu et al., "Reducing capacity and voltage decay of Co-free $Li_{1.2}Ni_{0.2}Mn_{0.6}O_2$ as positive electrode material for lithium batteries employing an ionic liquid-based electrolyte." *Adv. Energy Mater.*, **10**, 2001830 (2020).
14. C. J. Chen, W. K. Pang, T. Mori, V. K. Peterson, N. Sharma, P. H. Lee, S. H. Wu, C. C. Wang, Y. F. Song, and R. S. Liu, "The origin of capacity fade in the $Li_2MnO_3{\cdot}LiMO_2$ (M = Li, Ni, Co, Mn) microsphere positive electrode: an operando neutron diffraction and transmission X-ray microscopy study." *J. Am. Chem. Soc.*, **138**, 8824 (2016).
15. A. R. Armstrong, M. Holzapfel, P. Novák, C. S. Johnson, S. H. Kang, M. M. Thackeray, and P. G. Bruce, "Demonstrating oxygen loss and associated structural reorganization in the lithium battery cathode $Li[Ni_{0.2}Li_{0.2}Mn_{0.6}]O_2$." *J. Am. Chem. Soc.*, **128**, 8694 (2006).
16. D. Mohanty, S. Kalnaus, R. A. Meisner, K. J. Rhodes, J. Li, E. A. Payzant, D. L. Wood, and C. Daniel, "Structural transformation of a lithium-rich $Li_{1.2}Co_{0.1}Mn_{0.55}Ni_{0.15}O_2$ cathode during high voltage cycling resolved by in situ X-ray diffraction." *J. Power Sources*, **229**, 239 (2013).
17. W. Liu, P. Oh, X. Liu, S. Myeong, W. Cho, and J. Cho, "Countering voltage decay and capacity fading of lithium-rich cathode material at 60 °C by hybrid surface protection layers." *Adv. Energy Mater.*, **5**, 1 (2015).
18. B. Xu, C. R. Fell, M. Chi, and Y. S. Meng, "Identifying surface structural changes in layered Li-excess nickel manganese oxides in high voltage lithium ion batteries: a joint experimental and theoretical study." *Energy Environ. Sci.*, **4**, 2223 (2011).
19. P. K. Nayak, J. Grinblat, M. Levi, B. Markovsky, and D. Aurbach, "Structural and electrochemical evidence of layered to spinel phase transformation of Li and Mn rich layered cathode materials of the formulae $XLi[Li_{1/3}Mn_{2/3}]O_2.(1\text{-}x)LiMn_{1/3}Ni_{1/3}Co_{1/3}O_2$ (x = 0.2, 0.4, 0.6) upon cycling." *J. Electrochem. Soc.*, **161**, A1534 (2014).
20. K. S. Park, M. H. Cho, S. J. Jin, K. S. Nahm, and Y. S. Hong, "Effect of Li ion in transition metal sites on electrochemical behavior of layered lithium manganese oxides solid solutions." *Solid State Ionics*, **171**, 141 (2004).
21. F. Wu, G. T. Kim, M. Kuenzel, H. Zhang, J. Asenbauer, D. Geiger, U. Kaiser, and S. Passerini, "Elucidating the effect of iron doping on the electrochemical performance of cobalt-free lithium-rich layered cathode materials." *Adv. Energy Mater.*, **9**, 1902445 (2019).
22. J. Li, R. Klöpsch, M. C. Stan, S. Nowak, M. Kunze, M. Winter, and S. Passerini, "Synthesis and electrochemical performance of the high voltage cathode material $Li[Li_{0.2}Mn_{0.56}Ni_{0.16}Co_{0.08}]O_2$ with improved rate capability." *J. Power Sources*, **196**, 4821 (2011).
23. C. C. Wang and A. Manthiram, "Influence of cationic substitutions on the first charge and reversible capacities of lithium-rich layered oxide cathodes." *J. Mater. Chem. A*, **1**, 10209 (2013).
24. E. Zhao, X. Liu, H. Zhao, X. Xiao, and Z. Hu, "Ion conducting Li_2SiO_3-coated lithium-rich layered oxide exhibiting high rate capability and low polarization." *Chem. Commun.*, **51**, 9093 (2015).
25. E. Zhao, X. Liu, Z. Hu, L. Sun, and X. Xiao, "Facile synthesis and enhanced electrochemical performances of Li_2TiO_3-coated lithium-rich layered $Li_{1.13}Ni_{0.30}Mn_{0.57}O_2$ cathode materials for lithium-ion batteries." *J. Power Sources*, **294**, 141 (2015).
26. V. Aravindan, Y. S. Lee, and S. Madhavi, "Best practices for mitigating irreversible capacity loss of negative electrodes in Li-ion batteries." *Adv. Energy Mater.*, **7**, 1 (2017).
27. C. Xin, J. Gao, R. Luo, and W. Zhou, "Prelithiation reagents and strategies on high energy lithium-ion batteries." *Chem. Eur. J.*, **28**, e202104282 (2022).
28. D. Shanmukaraj, S. Grugeon, S. Laruelle, G. Douglade, J. M. Tarascon, and M. Armand, "Sacrificial salts: compensating the initial charge irreversibility in lithium batteries." *Electrochem. Commun.*, **12**, 1344 (2010).
29. S. Solchenbach, M. Wetjen, D. Pritzl, K. U. Schwenke, and H. A. Gasteiger, "Lithium oxalate as capacity and cycle-life enhancer in LNMO/Graphite and LNMO/SiG full cells." *J. Electrochem. Soc.*, **165**, A512 (2018).
30. A. Manthiram, J. C. Knight, S. T. Myung, S. M. Oh, and Y. K. Sun, "Nickel-rich and lithium-rich layered oxide cathodes: progress and perspectives." *Adv. Energy Mater.*, **6**, 1501010 (2016).

31. F. Klein et al., "Enhanced electrochemical capacity of spherical Co-free $Li_{1.2}Mn_{0.6}Ni_{0.2}O_2$ particles after a water and acid treatment and its influence on the initial gas evolution behavior." *Chem. Sus. Chem*, **15**, e202201061 (2022).
32. C. P. Aiken, J. Xia, D. Y. Wang, D. A. Stevens, S. Trussler, and J. R. Dahn, "An apparatus for the study of in situ gas evolution in Li-ion pouch cells." *J. Electrochem. Soc.*, **161**, A1548 (2014).
33. Z. Jusys, M. Binder, J. Schnaidt, and R. J. Behm, "A novel DEMS approach for studying gas evolution at battery-type electrodelelectrolyte interfaces: high-voltage $LiNi_{0.5}Mn_{1.5}O_4$ cathode in ethylene and dimethyl carbonate electrolytes." *Electrochim. Acta*, **314**, 188 (2019).
34. S. Radloff, L. S. Kremer, A. Hoffmann, and M. Wohlfahrt-Mehrens, "Characterization of structured ultra-thick $LiNi_{0.6}Co_{0.2}Mn_{0.2}O_2$ lithium-ion battery electrodes by mercury intrusion porosimetry." *Mater. Today Commun.*, **28**, 102549 (2021).
35. K. J. Carroll, D. Qian, C. Fell, S. Calvin, G. M. Veith, M. Chi, L. Baggetto, and Y. S. Meng, "Probing the electrode/electrolyte interface in the lithium excess layered oxide $Li_{1.2}Ni_{0.2}Mn_{0.6}O_2$." *Phys. Chem. Chem. Phys.*, **15**, 11128 (2013).
36. N. Yabuuchi, K. Yoshii, S. T. Myung, I. Nakai, and S. Komaba, "Detailed studies of a high-capacity electrode material for rechargeable batteries, Li_2MnO_3-$LiCo_{1/3}Ni_{1/3}Mn_{1/3}O_2$." *J. Am. Chem. Soc.*, **133**, 4404 (2011).
37. J. Wang, X. He, E. Paillard, N. Laszczynski, J. Li, and S. Passerini, "Lithium- and manganese-rich oxide cathode materials for high-energy lithium ion batteries." *Adv. Energy Mater.*, **6**, 1600906 (2016).
38. C. S. Johnson, J. S. Kim, C. Lefief, N. Li, J. T. Vaughey, and M. M. Thackeray, "The significance of the Li_2MnO_3 component in 'composite' $XLi_2MnO_3{\cdot}(1\text{-}x)LiMn_{0.5}Ni_{0.5}O_2$ Electrodes." *Electrochem. Commun.*, **6**, 1085 (2004).
39. J. Heitbaum and O. Wolter, "Differential electrochemical mass spectroscopy (DEMS)—a new method for the study of electrode processes." *Berichte der Bunsengesellschaft für Phys. Chemie*, **88**, 2 (1984).
40. P. Novák, J. C. Panitz, F. Joho, M. Lanz, R. Imhof, and M. Coluccia, "Advanced in situ methods for the characterization of practical electrodes in lithium-ion batteries." *J. Power Sources*, **90**, 52 (2000).
41. R. Imhof and P. Novák, "In situ investigation of the electrochemical reduction of carbonate electrolyte solutions at graphite electrodes." *J. Electrochem. Soc.*, **145**, 1081 (1998).
42. Z. Jusys and R. J. Behm, "Differential electrochemical mass spectrometry." *Encyclopedia of Electrochemical Power Sources', Reference Module in Chemistry, Molecular Sciences and Chemical Engineering*, ed. J. Garche and S. Brimaud (Elsevier B.V., Amsterdam) 2nd ed., Vol. 2, 77 (2025).
43. S. Shen et al., "Tuning electrochemical properties of Li-rich layered oxide cathodes by adjusting Co/Ni ratios and mechanism investigation using in situ X-ray Di Ff raction and online continuous flow Di Ff erential electrochemical mass spectrometry." *ACS Appl. Mater. Interfaces*, **10**, 12666 (2018).
44. B. Strehle, K. Kleiner, R. Jung, F. Chesneau, M. Mendez, H. A. Gasteiger, and M. Piana, "The role of oxygen release from Li- and Mn-rich layered oxides during the first cycles investigated by on-line electrochemical mass spectrometry." *J. Electrochem. Soc.*, **164**, A400 (2017).
45. N. Guerrini, L. Jin, J. G. Lozano, K. Luo, A. Sobkowiak, K. Tsuruta, F. Massel, L. C. Duda, M. R. Roberts, and P. G. Bruce, "Charging mechanism of Li_2MnO_3." *Chem. Mater.*, **32**, 3733 (2020).
46. (2024), NIST Chemistry WebBook https://webbook.nist.gov/cgi/cbook.cgi?ID=C7789200&Mask=80 accessed Sep 8.
47. R. A. Quinlan, Y-C. Lu, Y. Shao-Horn, and A. N. Mansour, "XPS studies of surface chemistry changes of $LiNi_{0.5}Mn_{0.5}O_2$ electrodes during high-voltage cycling." *J. Electrochem. Soc.*, **160**, A669 (2013).
48. A. N. Mansour, D. G. Kwabi, R. A. Quinlan, Y-C. Lu, and Y. Shao-Horn, "Probing the electrode-electrolyte interface in Cycled $LiNi_{0.5}Mn_{1.5}O_4$ by XPS using Mg and synchrotron X-rays." *J. Electrochem. Soc.*, **163**, A2911 (2016).
49. A. G. Kochur, A. T. Kozakov, A. V. Nikolskii, K. A. Googlev, A. V. Pavlenko, I. A. Verbenko, L. A. Reznichenko, and T. I. Krasnenko, "Journal of electron spectroscopy and valence state of the manganese ions in mixed-valence $La_{1-\alpha}Bi_{\beta}Mn_{1+\delta}O_{3\pm\gamma}$ Ceramics by Mn 2p and Mn 3s X-ray photoelectron spectra." *J. Electron Spectros. Relat. Phenomena*, **185**, 175 (2012).
50. G. G. Eshetu, T. Diemant, M. Hekmatfar, S. Grugeon, R. J. Behm, S. Laruelle, M. Armand, and S. Passerini, "Impact of the electrolyte salt anion on the solid electrolyte interphase formation in sodium ion batteries." *Nano Energy*, **55**, 327 (2019).
51. K. Edström, T. Gustafsson, and J. O. Thomas, "The cathode-electrolyte interface in the Li-ion battery." *Electrochimica Acta*, **50**, 397 (2004).
52. F. Klein, C. Pfeifer, J. Bansmann, Z. Jusys, R. J. Behm, M. Wohlfahrt-Mehrens, M. Lindén, and P. Axmann, "Effect of three-in-one surface modification of spherical, Co-free Li-rich cathode material for Li-ion batteries ($Li_{1.2}Mn_{0.6}Ni_{0.2}O_2$) with citric acid." *J. Electrochem. Soc.*, **169**, 120533 (2022).
53. R. S. Sánchez-Carrera and B. Kozinsky, "Computational raman spectroscopy of organometallic reaction products in lithium and sodium-based battery systems." *Phys. Chem. Chem. Phys.*, **16**, 24549 (2014).
54. H. G. M. Edwards and I. R. Lewis, "FT-raman spectroscopic studies of metal oxalates and their mixtures." *Spectrochim. Acta Part A Mol. Spectrosc.*, **50**, 1891 (1994).
55. J. Kim, O. B. Chae, and B. L. Lucht, "Perspective—Structure and stability of the solid electrolyte interphase on silicon anodes of lithium-ion batteries." *J. Electrochem. Soc.*, **168**, 030521 (2021).
56. M. Nie, D. P. Abraham, Y. Chen, A. Bose, and B. L. Lucht, "Silicon solid electrolyte interphase (SEI) of lithium ion battery characterized by microscopy and spectroscopy." *J. Phys. Chem. C*, **117**, 13403 (2013).
57. D. Aurbach, H. Teller, M. Koltypin, and E. Levi, "On the behavior of different types of graphite anodes." *In Journal of Power Sources*, **119–121**, 2 (2003).